Naval Research Laboratory
Washington, DC 20375-5320

NRL/8220/MR—2021/2

Advanced Optical Diagnostics in Hypersonic Flows

JONATHAN SOSA, PH.D

Spacecraft Engineering Branch
Naval Center for Space Technology Division

February 10, 2022

REPORT DOCUMENTATION PAGE

Form Approved
OMB No. 0704-0188

1. REPORT DATE *(DD-MM-YYYY)*	**2. REPORT TYPE**	**3. DATES COVERED** *(From - To)*
10-02-2022	NRL Memorandum Report	Nov 11, 2019 – Nov 11, 2021

4. TITLE AND SUBTITLE

Advanced Optical Diagnostics in Hypersonic Flows

5a. CONTRACT NUMBER

5b. GRANT NUMBER

5c. PROGRAM ELEMENT NUMBER
NISE

6. AUTHOR(S)

Jonathan Sosa, Ph.D

5d. PROJECT NUMBER

5e. TASK NUMBER

5f. WORK UNIT NUMBER
N2W2

7. PERFORMING ORGANIZATION NAME(S) AND ADDRESS(ES)

Naval Research Laboratory
4555 Overlook Avenue, SW
Washington, DC 20375-5320

8. PERFORMING ORGANIZATION REPORT NUMBER

NRL/8220/MR--2021/2

9. SPONSORING / MONITORING AGENCY NAME(S) AND ADDRESS(ES)

Naval Research Laboratory
4555 Overlook Avenue, SW
Washington, DC 20375-5320

10. SPONSOR / MONITOR'S ACRONYM(S)

NRL-NISE

11. SPONSOR / MONITOR'S REPORT NUMBER(S)

12. DISTRIBUTION / AVAILABILITY STATEMENT

DISTRIBUTION STATEMENT A: Approved for public release; distribution is unlimited.

13. SUPPLEMENTARY NOTES

Karles Fellowship

14. ABSTRACT

This work aims to investigate and establish optical diagnostics techniques for the U.S. Naval Research Laboratory's (NRL) Variable-Speed Hypersonic Wind Tunnel (HSWT) during the two year Karles Fellowship. Stereoscopic planar laser Rayleigh scattering of CO2 particles, typically several nanometers to tens of nanometers in size, were used in this study allowing cross-sectional visualization of the supersonic flow and turbulent boundary layers throughout the test section of the U.S. Naval Academy Supersonic Wind Tunnel. The optical diagnostic measurements show asymmetric boundary layer growth between the top and bottom walls of the test section as well as a disturbed bottom boundary layer due to the induced pressure and velocity gradient.

15. SUBJECT TERMS

16. SECURITY CLASSIFICATION OF:			**17. LIMITATION OF ABSTRACT**	**18. NUMBER OF PAGES**	**19a. NAME OF RESPONSIBLE PERSON**
					Jonathan Sosa, Ph.D
a. REPORT	**b. ABSTRACT**	**c. THIS PAGE**	U	43	**19b. TELEPHONE NUMBER** *(include area code)*
U	U	U			(202) 404-3080

Standard Form 298 (Rev. 8-98)
Prescribed by ANSI Std. Z39.18

This page intentionally left blank.

CONTENTS

This page intentionally left blank.

ADVANCED OPTICAL DIAGNOSTICS IN HYPERSONIC FLOWS

1. INTRODUCTION

1.1 Historical Perspective

Revitalized interest in hypersonic and space technologies has substantially increased the demand for improvements in optical diagnostics. Since the start of the new century, there has been rapid increase in the development of diagnostics for both reacting and non-reacting high-speed air flows. The development of new ultra-short pulse and burst-mode lasers, both with higher power and pulse energy, as well as high-speed and high-resolution cameras, timing and synchronization systems, and enhanced detectors has brought forth new capabilities [1]. The use of optical diagnostics to probe high-speed flows dates backs as far as the 1800s, where shadowgraphs and schlieren imaging were used to image shock-waves, Mach disks, and other naturally occurring fluid structures in compressible flows [2]. Progress in optical diagnostics through the twentieth century was mainly geared towards the advancement of schlieren and shadowgraph techniques with focus on improving density gradient sensitivity and image resolution. The main issue with schlieren and shadowgraph techniques stems from the integration of light over the full optical path length, leading to proper resolution of large scale structures such as shock waves, but loss of detail for finer resolution and dynamically variant structures such as turbulent boundary layers, shear layers, mixing layers, and highly transient shock systems [1]. Early use of electron beams partially resolved these issues due to the ability of spatially collimating the beam, providing luminescent cross sections of shock and boundary layer structures. However, electron beams are limited to very low density flows due to electron scattering, and become incredibly difficult if not impossible to integrate into certain types of test facilities [3].

Since the invention of the laser in 1960, advances in optical diagnostics have been largely driven by improvements in laser and camera capabilities. The pulsed ruby laser was the first laser invented and provided high energy and illumination coherence, this led to the early use of holographic techniques to measure flow field properties, such as multiple exposure holographs of seeded particles to measure flow velocity [4] or measurements of density variations in separated supersonic boundary layers [5]. The limitation was that the pulsed ruby laser could only achieve narrow wavelength bands. With the invention of the frequency tunable laser and organic dye lasers in 1966, spectroscopy as well as atomic and molecularly excited visualizations became possible [6, 7]. These early tunable dye lasers were only efficient in certain wavelengths of the visible spectrum, thus requiring seeding the flows to be able to appropriately excite a given species and probe them. Early experiments used sodium as seed, and tuning the laser onto or near a resonant wavelength allowed for laser-induced fluorescence of the excited seed in order to image planar cross sections. The ability to tune the laser wavelength also enabled velocimetry measurements taking advantage of the Doppler shift associated with the gas pressure, temperature, and velocity changes in hypersonic sodium-seeded helium flows [8, 9].

Given the reactivity of sodium in air, additional non-reactive tracers were sought for use in subsonic and supersonic air flows. Molecular iodine was one of the first tracers to be used in air for laser-induced fluorescence flow imaging of a supersonic jet using an argon-ion laser [10]. Further developments to tunable lasers through frequency conversion and nanosecond pulsed dye lasers gave rise to tunable ultraviolet lasers which allowed for the use of other tracer species such as nitric oxide (NO) [11] and acetone [12] as seed in laser-induced fluorescence experiments.

More recently, the use of non-linear optical methods has become possible due to the progress in higher power, higher energy, frequency tunable pulsed lasers. For example, temperature and species measurements of flows has become possible by Coherent Anti-Stokes Raman Scattering (CARS) [13], temperature and velocity measurements via Laser Induced Thermal Anemometry (LITA) [14], and Molecular Tagging Velocimetry (MTV) [15]. CARS brings two or three pulsed laser beams together at a point, and through resonant non-linear interaction, generates an additional laser beam with properties dependent on the gas medium at that point. CARS is particularly sensitive to temperature and species concentrations of the gas

Manuscript approved December 17, 2021.

being probed, thus it is of particular interest in hypersonic and propulsion related applications. Originally, the CARS technique required that at least one of the lasers be scanned in frequency to acquire data and this meant CARS could only provide time-averaged data. Later, broadband and dual-broadband CARS replaced the frequency scanned laser with a broadband laser which allowed multiple CARS signal frequencies to be split and generated, and simultaneously collected with a spectrometer. This enabled full spectral data to be collected in a single pulse and is the principle to the modern variants of CARS [16]. LITA is similarly reliant on focusing a pair of lasers to a point to produce localized thermal grating in air via non-linear mixing, and probing the laser to follow the motion of the acoustic waves created. This provides a local temperature through the measurement of the speed of sound from the acoustic waves and the flow velocity through the frequency offset associated with the fluid motion [14].

Unlike CARS and LITA, MTV introduces a line, or an array of lines of a molecularly excited species into the flow, and tracks them through time to provide a measurement of flow velocity and flow structure [15]. The first attempt at MTV in unseeded air was through Raman Excitation and Laser Induced Fluorescence (RELIEF), using two lasers. The first laser used Raman excitation to drive oxygen in the air into a vibrationally excited state, and the second used laser-induced fluorescence of the vibrationally excited oxygen to spatially track the fluorescent line [17]. The successful demonstration of RELIEF led to the excitation of other species such as Ozone Tagging Velocimetry (OTV), using laser-induced dissociation of molecular oxygen to create and track ozone in unseeded air flows with a two laser approach similar to RELIEF [18]. Around the same time other MTV approaches for air used seed such as biacetyl [19] and water vapor [20] to generate the fluorescent lines for tracking.

Unlike molecularly excited approaches, other laser diagnostics rely and have relied on using seeded particles in flows to provide quantitative measurements through tracking, holographic imaging, or interferometric methods. Much of the early work focusing on the use of particles for flow probing was Laser Doppler Anemometry (LDA), also commonly known as Laser Doppler Velocimetry (LDV). LDA/LDV makes use of two intersecting continuous wave lasers creating an interference pattern, as a particle passes through the intersection point, it disrupts the interference pattern and the velocity of the particle can be derived from the Doppler shift between the frequency of the incident and scattered laser light [21]. An added advantage of LDV is that the system could be expanded with additional laser pairs enabling two or three component velocity measurements. With the rise of nanosecond pulsed lasers, also came the rise of new optical diagnostics for flow velocimetry. The short nanosecond laser pulses could have timescales much shorter than the fluid convective velocity and are capable of essentially “freezing” the flow in time. Advancements in dual-pulsed nanosecond lasers and high-resolution CCD cameras, led to digital Particle Image Velocimetry (PIV), where two-dimensional images of light scattered from particles could be tracked between two frames, and the displacement between these particles could be measured to derive two-dimensional velocity fields [22, 23].

Starting the new century, many of the laser diagnostics used today already existed, or the foundation of these capabilities had been explored by early pioneer experiments. As camera and laser technology continues to advance, further development and implementation of these diagnostics continues to occur. For example, aside from higher pulse energies, faster and more reliable lasers, and higher resolution camera sensors, new developments in frequency tunable burst-mode lasers or lasers capable of sub-picosecond laser pulses have created new possibilities for optical diagnostics. These developments in particular have led to major advances in high-speed imaging, Particle Image Velocimetry, Laser Induced Fluorescence, Rayleigh Scattering, molecular flow tagging, and spectroscopy for hypersonic applications.

1.2 Objective

This work aims to investigate and establish optical diagnostics techniques for the U.S. Naval Research Laboratory's (NRL) Variable-Speed Hypersonic Wind Tunnel (HSWT) during the two year Karles Fellowship. The methods outlined, proposed, or developed under the Karles Fellowship will enable capabilities in experimental aerodynamics, turbulent boundary layers and turbulent transition, surface heating, reactive flow, and validation of numerical simulation codes.

1.3 Report Contents

Chapter 2 provides a brief literature review of modern optical diagnostics and their application in supersonic and hypersonic flows, with emphasis on recent advancements in the field and new enabling equipment and techniques developed. Chapter 2 is broken down into multiple sub-categories each highlighting a different set of diagnostic techniques and recent investigations from each as applied to high-speed compressible flows.

Chapter 3 discusses experiments performed at the U.S. Naval Academy to show the application of high-speed schlieren imaging and CO_2 Rayleigh scattering diagnostics discussed in Chapter 2 as applied to characterization of the upcoming NCST Variable Mach Number Hypersonic Wind Tunnel. Chapter 3.1 presents a CO_2 Rayleigh scatter imaging investigation to characterize turbulent boundary layer growth and flow quality in the U.S. Naval Academy Wind Tunnel.

Chapter 4 summarizes the results of this report and presents future work and recommendations for the development of relevant optical diagnostics for the NCST Hypersonic Wind Tunnel.

2. LITERATURE REVIEW

This section provides a brief overview of the recent progress in modern optical diagnostics, particular emphasis is given to diagnostics with applications in blowdown wind tunnels and propulsion experiments. Each section highlights a different suite of diagnostics and new developments that have enabled unique capabilities in probing hypersonic flows.

2.1 Schlieren & Shadowgraph Techniques

2.1.1 Overview

Schlieren and shadowgraph imaging are optical techniques that rely on precisely aligned optics to image refractive disturbances in transparent mediums. Robert Hooke formally originated the concept of schlieren and shadowgraph imaging in the 17th century [24]. Later in the mid-19th century, August Toepler reinvented the schlieren technique with more modern optics and it became a standard laboratory tool mainly with widespread use in wind-tunnel testing. Today the use of both schlieren and shadowgraph techniques is widespread across scientific experimentation [25]. The goal of this section is to highlight the major advances of both schlieren and shadowgraph techniques as applied to hypersonic and propulsion related efforts, particularly the development of these due to advances in modern optics, digital imaging, and digital processing.

The underlying theory supporting schlieren and shadowgraph imaging is based on geometrical optics with consideration of diffraction effects. The Gladstone-Dale law generally describes the simplified relationship between a fluid of density (ρ), its refractive index (η), and fluid specific constant *k*, highlighted in Equation 1.

$$\eta - 1 = k\rho \qquad \text{Equation 1}$$

As the refractive index changes due to the density disturbances, the light and dark patterns seen in a schlieren image do not relate directly to the refractive index (η), but instead to the gradient of the refractive index $\delta\eta/\delta x$ and $\delta\eta/\delta y$ perpendicular to the orientation of the knife edge in the schlieren system. For a shadowgram, the second spatial derivative is displayed.

2.1.2 Shadowgraph & Schlieren Imaging

A simplified schematic of the two most popular schlieren arrangements, the Toepler lens-type and z-type schlieren systems are shown in Figure 1. Figure 1 (A) shows the schlieren setup first developed by Toepler [26]. A "point" light source (LS) is collimated by the first lens (L1) and brought to a focal point by the second lens (L2). At the focal point created by L2, a sharp knife-edge (KE) is placed to block a fraction of the light and is then captured by the camera to image the density disturbance (S) placed in the optical path. Similarly, the z-type schlieren setup replaces the collimating and focusing lenses L1 and L2 with off-axis parabolic mirrors PM1 and PM2 to achieve the same effect. In general, the light rays passing through the schlieren object are defracted due to the density disturbances of the medium, and either avoid or collide with the knife edge. This allows the setup to capture phase disturbances as gray-scale intensities on the camera sensor. It's also important to note that both of these setups are capable of producing shadowgrams by removing the knife edge and defocusing the camera lens from the schlieren object.

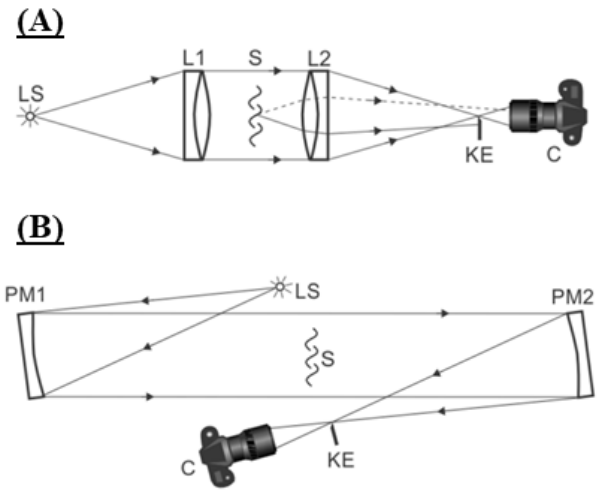

Figure 1 Representation of (A) Toepler's lens-type schlieren system (B) Z-Type schlieren system using parabolic mirrors, adapted from [25].

A newer generation of cameras and light sources has allowed for simultaneously faster, higher resolution, and clearer schlieren and shadowgraph images. For example, new digital cameras with CMOS sensors, such as the Photron Fastcam SA-Z or the Vision Research Phantom V2512, can nowadays easily and reliably provide megapixel resolution at 20,000 frames per second (fps) or peak frame rates going beyond 1,000,000 fps at reduced resolution. More recent developments in high speed cameras by Shimadzu and Kirana can reach peak recording rates of 5 – 10 million fps, at the cost of at most only recording a couple hundred frames.

Aside from more obvious applications such as investigating shock structures and large scale features in supersonic and hypersonic flows, the use of short-exposure, high-speed schlieren imaging has been extensively used and proven in the case of hypersonic boundary layer transition. Recently, in 2012, Laurence et al. used high-speed schlieren to visualize the instability waves in a hypersonic boundary layer on a cone model in a time resolved fashion. A Toepler type dual lens schlieren system like the one shown in Figure 1 (A) was used, paired with a Shimadu HPV-1 camera and a 1000 W short-arc Xenon lamp to achieve recording rates up to 1 MHz [27]. The experiments were carried out in a high-enthalpy shock tube at the German Aerospace Center using a 1.1m meter 7° half-angle cone at a Mach number of 7.3. Figure 2 highlights the cone model and an example schlieren image of the boundary layer undergoing transition. Recording at 500 kfps it is possible to visually track the wave packets as the boundary layer undergoes transition, forming near the rightmost side of the interrogation region. The authors propose that using a line probe of pixel average intensities parallel to the cone surface, it is possible to derive frequency propagation characteristics of boundary layer instabilities.

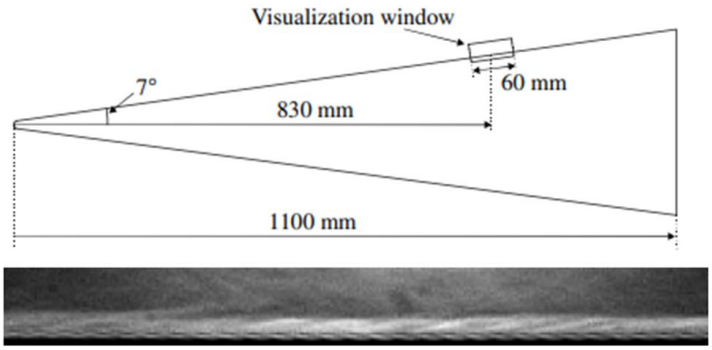

Figure 2 Schematic of cone model and schlieren interrogation region (top) and schlieren image of transitioning boundary layer (bottom) adapted from [27].

Later experiments by Laurence et al. sought to improve the schlieren techniques used for the boundary layer transition experiments by reversing the roles of the camera and light source. Instead of using a high-speed camera with a continuous light source as done for the prior experiments [27], a pulsed light source allowed the use of a higher-resolution lower speed camera while still "freezing" the flow. For these experiments a higher resolution Phantom v641 camera was recording at 64 kfps, with a resolution of 1408 x 40 pixels, as compared to the previously recoded images at a fixed resolution of 312 x 260 pixels with the Shimadzu camera. The light source used was a Cavilux Smart visualization laser, allowing short laser pulses on the order of 10 ns, with adjustable pulse separation allowing sequential image pairs to be captured [28]. Figure 3 highlights an image pair of the hypersonic boundary layer with a time separation of 2.8 μs between both images. Aside from the timing advantages the Cavilux Smart laser offers, another advantage of the ultra-short pulsed light source with respect to other lasers is the beam incoherence providing speckle free images. For comparison, boundary layer transition experiments at the Von Karman Institute Mach 6 Wind Tunnel, VKI H3, used a more convenitional Quantel Nd:YAG pulsed laser as the light source, with a laser pulse width of 8 ns [29]. In order to adequately use the laser as a schlieren light source for this case, the use of a fluorescent material that gives off light when struck by a laser is required instead of illumination from the coherent laser light source. The direct use of the laser would lead to a speckled pattern image with interference that would essentially render the imaging technique useless. Figure 4 highlights the modifications required to the Toepler type schlieren setup to enable the use of a coherent laser light source as well as a sample schlieren image of the transitional boundary layer on a 7° cone at Mach 6 with a Reynolds number of 22.6 x 10^6/m.

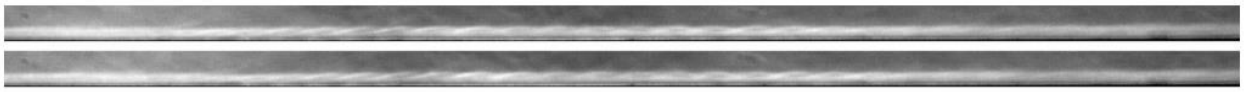

Figure 3 Schlieren images using laser light source of hypersonic boundary layer (M=7.4) with wave packets present. Time separation between the images is 2.8 μs. Adapted from [28].

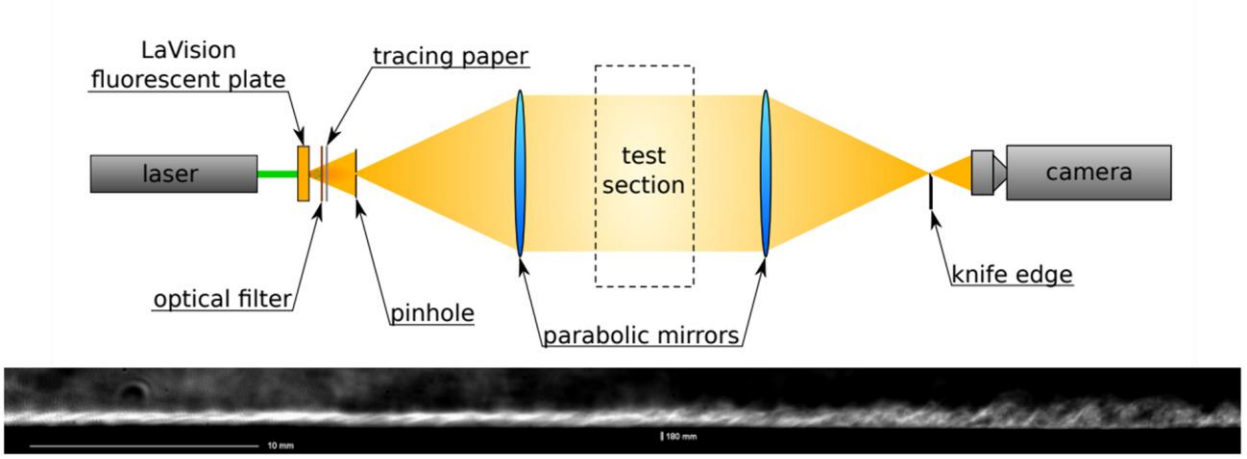

Figure 4 Schematic of the laser-based schlieren setup at VKI-H3 (top) Example schlieren image using the laser-based schlieren setup. Adapted from [29].

Similar experiments were carried out at the Sandia Hypersonic Wind Tunnel (HWT) by Casper et al. [30]. For this experimental campaign a 0.517m cone with a 7° half-angle was tested at Mach 5, 8, and 14 over a range of *Re* to catalog the disturbances in the boundary layer over a broader condition set. Simultaneous pressure measurements taken at 5 axial locations along the surface of the cone and a Toepler type schlieren setup using a Flashpoint II 1220A Monolight and a Phantom v12.1 camera were used to characterize the boundary layer. Figure 5 highlights the experimental setup for the Sandia HWT as well as representative images for the three Mach numbers tested at similar Reynolds numbers. At Mach 5, low frequencies disturbances would occasionally develop in the otherwise laminar boundary layer. The Mach 8 boundary layer disturbances are dominate by second-mode instabilities at these Reynold numbers. At Mach 14, similar second-mode instabilities were only observed at the lower Reynolds numbers before breaking down into turbulence at higher Reynolds numbers.

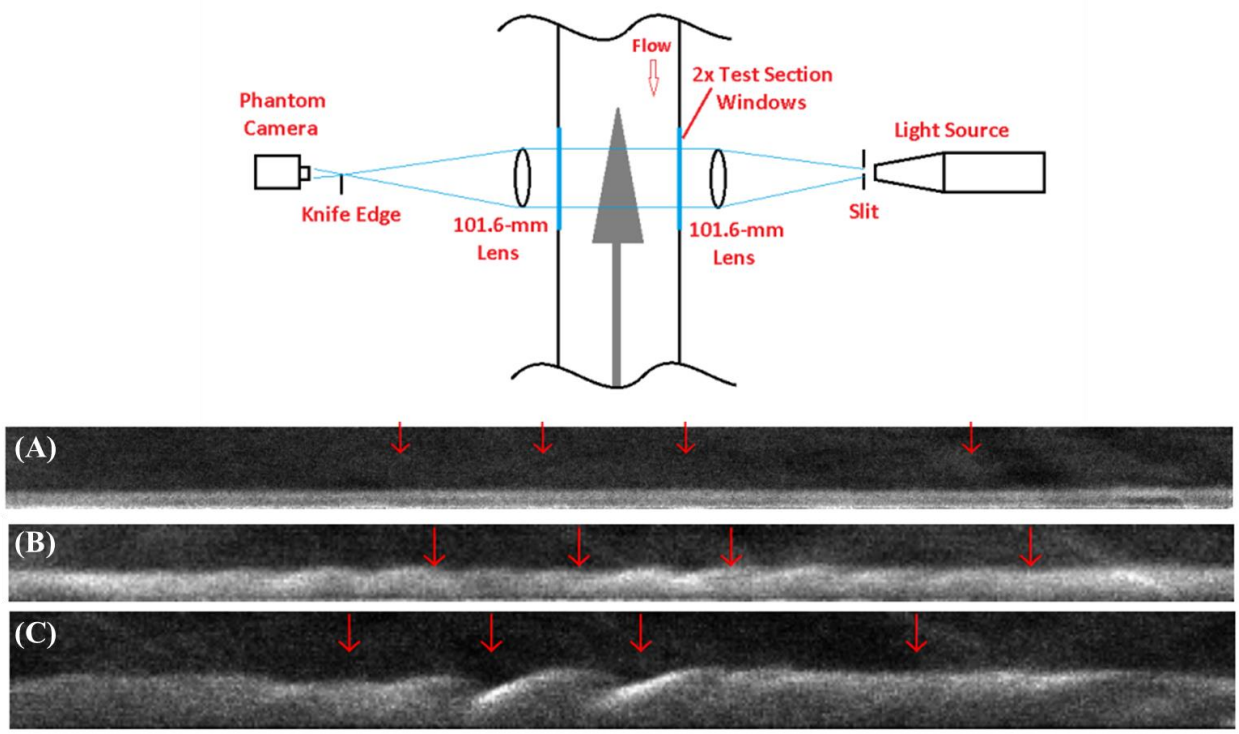

Figure 5 Schematic of the Sandia Hypersonic Wind tunnel high-speed schlieren system (top) (A) Laminar boundary layer M=4.95 Re=4.39 x 10^6/m (B) Boundary layer with second-mode wave packets M=7.8 Re=3.62 x 10^6/m (C) Boundary layer with intermittent wave packets M=14.4, Re=3.62 x 10^6/m. Adapted from [30].

2.1.3 Background Oriented Schlieren

The Background Oriented Schlieren (BOS) technique is one of the most recent developments in the schlieren field and has become largely popular due to the advances in speed and accuracy of computer image correlation techniques. BOS is also commonly referred to as synthetic schlieren due to the need of digital image processing to recreate the schlieren image. A typical BOS setup is shown in Figure 6. In BOS the camera (C) images a background with known (B) illuminated evenly while purposefully avoiding the schlieren object (S) by the light source (LS). An undistorted 'tare' (reference) image of the background is recorded and computationally compared to the speckled background distorted by the schlieren object. Digital image processing is able to measure the shifts between the images and from the shifts construct a pseudo-schlieren image without the need of any of the optics required in the schlieren setups shown in Figure 1(A) and (B). A recent review by Raffel [31] discusses the implementation and application of BOS in a broader fashion.

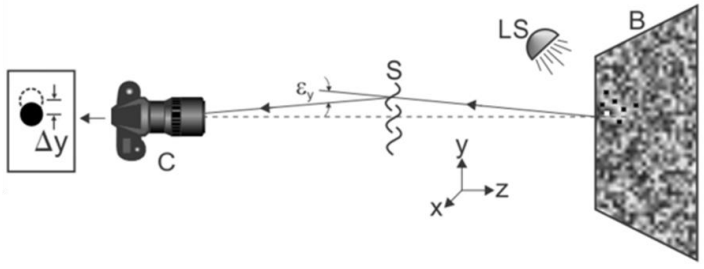

Figure 6 Schematic of speckled background Back Oriented Schlieren (BOS) setup. Adapted from [25].

One of the main advantages of BOS is avoiding the expensive and sensitive optics required to obtain schlieren images. This enables BOS to be used in applications or locations where Toepler type or z-type schlieren would traditionally be impossible to setup or perform. Recently, one of the more unique applications of BOS has been air-to-air BOS (AIRBOS). An observation aircraft carrying a camera images a target aircraft flying below it and uses naturally occurring speckles on the ground such as vegetation or rocky terrain as a speckled background. The most notable application of AIRBOS has been to image the shock structure of a T-38 flying over the desert near Edwards Air Force Base. Figure 7 highlights the instrumentation aboard the observation aircraft to record the BOS images for the T-38 in flight at Mach 1.05 as well as the speckle pattern created on the desert floor by creosote bushes found in the Mojave Desert.

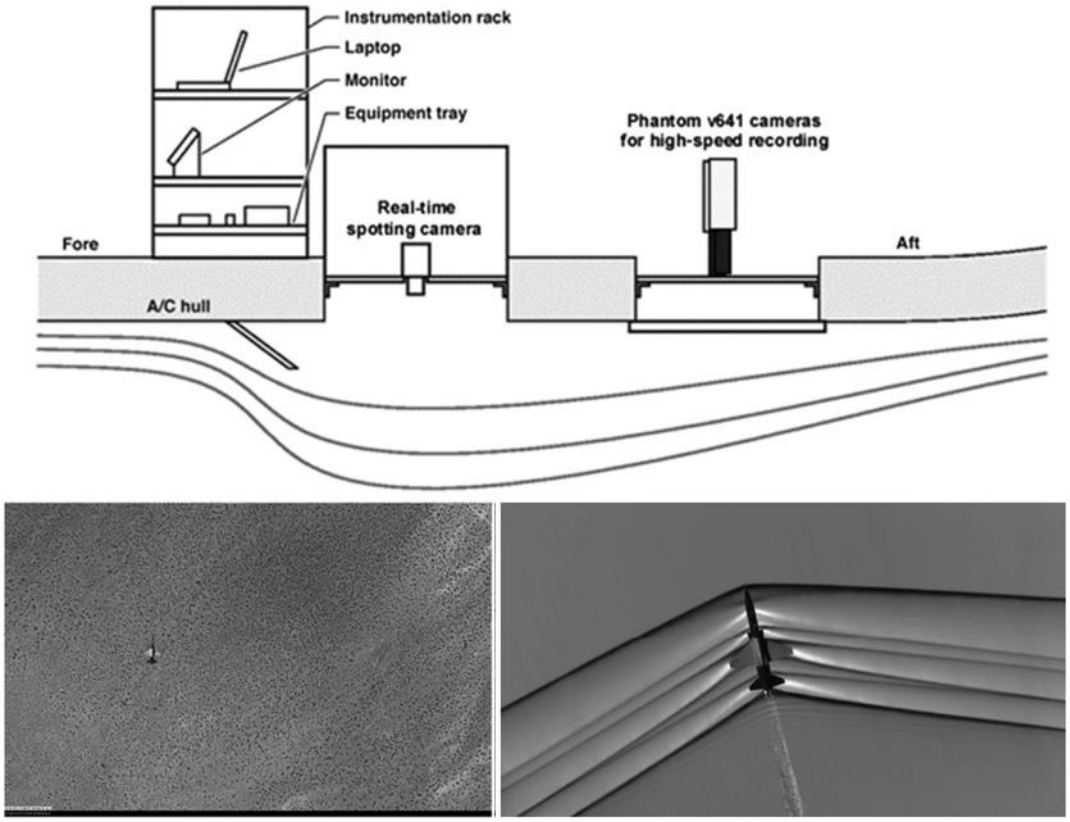

Figure 7 Imaging system aboard a Beechcraft B-200 aircraft for AIRBOS (top) Example images of naturally ocurring speckle and post-processed BOS image of T-38 aircraft (bottom). Adapted from [32].

The major disadvantage of BOS is the lower spatial resolution and sharpness as compared to schlieren images. Due to the particle image velocimetry like algorithms used for image cross correlation in BOS, a camera sensor resolution would need to be at least 2 to 4 times higher for an equivalent field of view to produce images of similar sharpness, not factoring any digital noise incurred in post-processing. Fisher et al. did a comparison between a conventional z-type schlieren system and BOS for an otherwise equivalent test at hypersonic speeds [33]. A flared cone model was chosen to generate a conical shock, expansion fans, shock-shock interactions, and a shear layer to compare the sensitivity of the two techniques at Mach 5. Figure 8 shows the schlieren images for both BOS and a z-type schlieren setup. Although BOS can resolve all the large scale features expected from the flow field, it is evident that the BOS data has lower spatial resolution and loses sharpness particularly resolving the aft compression and expansion. However, BOS can be useful for these applications to inform the areas where additional sensitivity may be needed to position knife edges strategically in optically based schlieren setups.

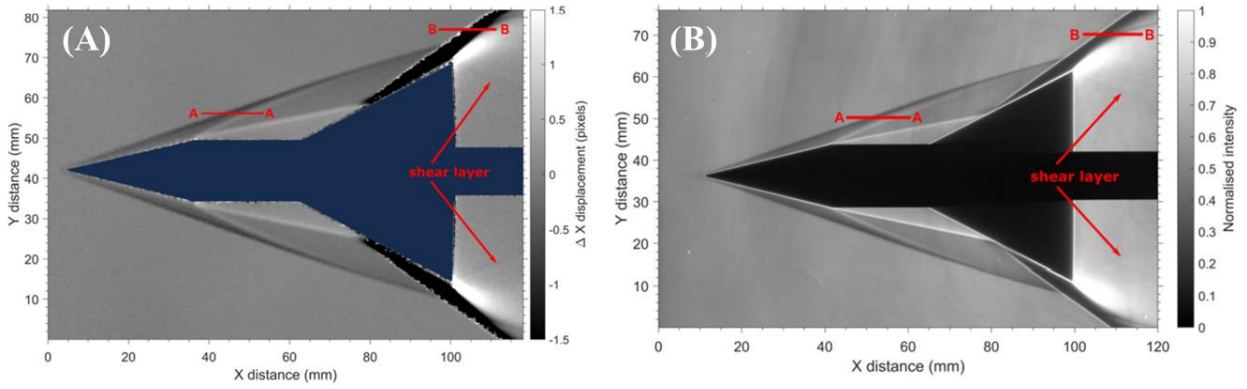

Figure 8 (A) BOS image of flared cone model (B) Z-type schlieren image of flared cone model. Adapted from [32].

2.1.4 Focusing Schlieren Techniques

The final common derivative of schlieren techniques is the focusing schlieren setups. Figure 9 shows the schematic of a "lens-and-grid" focusing schlieren setup originally proposed by Weinstein [34]. The focusing schlieren system can roughly be thought of as a composite of multiple schlieren setups passing through the schlieren object (S). In this case, the "light source" is source grid (SG) with known pattern. A series of several lamps (LS) provides the back lighting whose light is directed by a Fresnel lens (FL) through the source grid toward a schlieren lens (SL). This lens relays the image produced by the source grid and it is partially blocked by a cutoff grid (CG) which is a matching negative of the source grid and behaves as multiple knife edges. Lastly, a relay lens (RL) transmits the image onto the camera (C). The benefit of the focusing schlieren arrangement is a narrow depth of focus at the schlieren object, this bypasses the usual schlieren difficulty of integrating everything along the optical path into a 2D image.

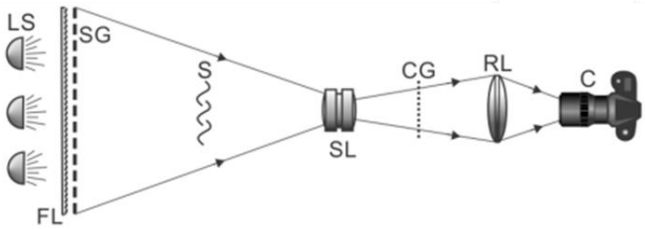

Figure 9 Schematic of lens and grid focusing schlieren setup. Adapted from [25].

The primary application of focused schlieren is flow visualization, the narrow depth of focus adds new possibilities to the traditional applications of the schlieren technique, particularly in situations where selective imaging in highly three-dimensional flows is desired. Furthermore, given the opportunity to image "planar" density fields, focusing schlieren is often coupled with deflectometry techniques to quantify high frequency density fluctuations at a given point in the flow field. VanDercreek discusses the simultaneous use of focusing schlieren and deflectometry at the U.S. Air Force Arnold Engineering Development Center (AEDC) Hypersonic Wind Tunnel Number 9 [35, 36]. The focusing schlieren technique developed for Tunnel 9 demonstrated a large field of view (25 cm), a narrow depth of focus (1 cm), and sensitivity capable of resolving transient boundary layer phenomena in hypersonic flows on cone models. Figure 10 shows an imagine obtained at Mach 10 at Tunnel 9 on a 7° half-angle transition cone, the focused schlieren image is capable of successfully resolving the second-mode waves traversing through the boundary layer of the cone model.

Figure 10 Focused schlieren image of Mach 10 boundary layer, Re = 2 x 10^6/ft. Adapted from [36].

2.2 Laser Scattering Techniques

2.2.1 Particle Image Velocimetry

Particle image velocimetry (PIV) is an optical flow diagnostic where the fluid motion is made visible by adding small tracer particles, laser light is then mie-scattered from the particles, and by imaging these particle fields at two instances in time with a known time increment, the particle displacement can be used to infer the flow velocity field. Figure 11 illustrates a simplified schematic of a traditional two-dimensional PIV setup for a wind tunnel. A plane within the flow seeded with particles, is illuminated twice by a dual-headed laser, pulsed with a known time delay. This time delay between pulses needs to be tailored depending on the flow velocity and image magnification, for hypersonic flows this can challenging due to the need of the pulse separation between laser heads to be on the order of magnitude of 10ns - 1µs. The light scattered by the particles is recorded on two separate frames on a digital camera sensor, and a cross correlation algorithm is used to estimate the particle displacement between two frames [37].

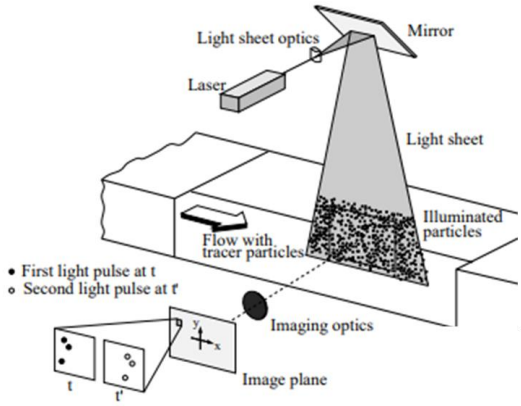

Figure 11 Typical experimental configuration for 2D particle image velocimetry in a wind tunnel. Adapted from [37].

For both supersonic and hypersonic applications on of the main concerns with particle image velocimetry is the particle drag the solid particulates used to seed the flow incur. Of particular interest is particle response to an oblique shock wave as a measure of the tracer time response to the velocity discontinuity across the shock wave. The motion of a small particle immersed in a moving gas is governed mostly by viscous drag and the inertial force it carries [38]. The equation of motion for a spherical particle with diameter d, moving at a velocity $\boldsymbol{V}$, being carried by a fluid of velocity $\boldsymbol{U}$ and viscosity $\boldsymbol{\mu}$, can be modeled as a function of the particle Reynolds number $\boldsymbol{Re_p}$, based on the particle diameter $\boldsymbol{d}$. Additionally, the particle density $\boldsymbol{\rho_p}$, and the drag coefficient $\boldsymbol{C_D}$ are specified to model the particle motion as highlighted in Equation 2.

$$\frac{dV}{dt} = -\frac{3}{4} C_D Re_p \frac{\mu}{\rho_p d_p^2} (V - U) \qquad \text{Equation 2}$$

To illustrate the dependence of particle size and specification of a drag coefficient model for any given particle, three increasingly complex drag models are used in a reference problem modeled by Equation 2, the first by Stokes assuming particle drag is constant [39], the second by Henderson which takes into consideration particles in continuum and rarified flows [40], and the third by Loth which takes into consideration flow compressibility and rarefaction effects [41]. For brevity the full differential form of the drag models aren't shown here and the reader is directed to the references for the full description. In addition, three particle sizes 1 μm, 10 μm, and 100 μm are modeled with the Loth drag model to highlight the effect of particles that track. The supersonic fluid is assumed to be moving at a consistent Mach number of 4 with a stagnation temperature of 295 K, the particles are assumed to be moving the same velocity as the fluid up until the shock generated by a 5° wedge. The particles are assumed to be perfectly spherical with a constant density of that of a water droplet (1000 kg/m^3).

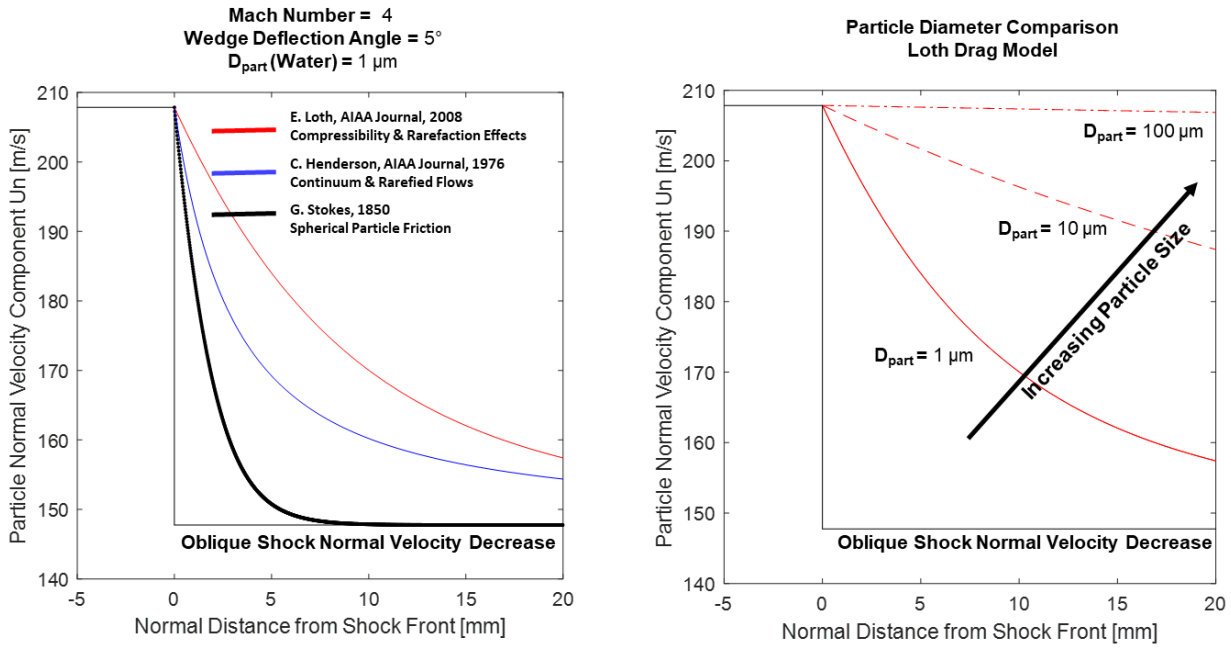

Figure 12 (Left) Effect of drag model on particle repsonse to an oblique shock at Mach 4 (Right) Particle size dependence on particle response.

Figure 12 shows the comparison between drag models and particle size for the oblique shock reference problem. From the variation in drag models it is evident that taking into consideration compressibility effects and relaxing the assumption that both the particle drag and Reynolds number are constant, leads to a more realistic representation of the particle motion through the shock wave. This emphasized the importance of selecting an appropriate drag model for the flow field of interest. Furthermore, particle size is the largest effector on particle shock response. For particles 1 μm or smaller, the particles tend towards reaching the post-shock velocity at distances slightly greater than 20mm. As particle size increases, for example 100 μm, the particle momentum is high enough where the particle essentially carries its original velocity through the shock front and fails to capture the velocity drop. This is of utmost importance in PIV measurements particularly for small models and short distances where the particle would impact the model at the original velocity and the fluid being probed would be inaccurately resolved based on tracking the particle movements.

The application of digitized PIV to supersonic and hypersonic flows has only been applied successfully since the turn of the century. Advances both in camera and laser technology have allowed interrogation of the ultra-high speeds, short time scales, and extreme thermodynamic conditions encountered in hypersonic flows. Schrijer et al. was one of the first to apply digital high-speed PIV to a hypersonic flow investigating a two-dimensional compression ramp in a Ludwieg tube at the Delft University of Technology [42]. A preliminary study on a reference ramp showed that 50 nm titanium dioxide particles yielded a relaxation time of 2.5 μs, sufficient to resolve the flow velocities seen on the 15° – 45° wedge placed in a Mach 7 flow. Figure 13 highlights a schlieren image and the velocity field derived from the PIV measurements. It can be see that the PIV measurements are capable of resolving all the large scale features shown, furthermore, under adiabatic flow assumptions, the Mach number distribution shown in Figure 13 is within 2% of the theoretical prediction and the shock angles derived from the PIV images are within 1° of the expected value. This study showed that given sufficiently small particle sizes and high enough spatial resolution, PIV data could provide quantitative measurements of the near wall regions of a hypersonic flow.

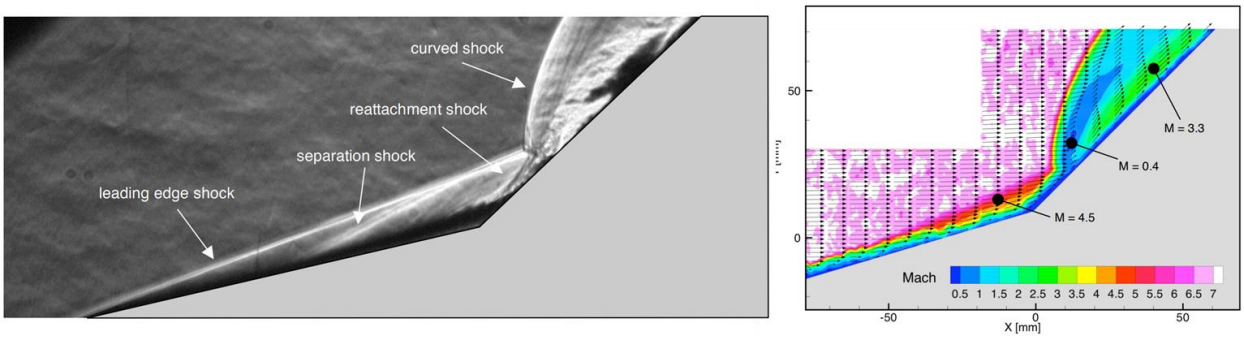

Figure 13 (Left) Schlieren image of the 15° - 45° wedge flow (Right) Corresponding PIV velocity field of the 15° - 45° wedge flow adapted from [42].

Following the successful implementation of planar PIV in hypersonic flows, Avallone et al. set out to expand the capability to three-dimensional PIV measurements, typically referred to as tomographic PIV, to investigate hypersonic laminar to turbulent boundary layer transition behind roughness elements at Mach 7.5 [43]. The experiments were also carried at a the Delft University of Technology Ludwieg tube, for these experiments the target Mach number was 7.5, with a total pressure and total temperature of P_0=28 bar and T_0=579 K. Figure 14 shows the wedge setup with the cylindrical roughness element placed 60 mm from the leading edge as well as the 3 camera tomographic setup. In order to generate a sufficiently illuminated laser volume, a Quantel Evergreen Nd:YAG laser with 200mJ/pulse delivers 10 ns pulses with a set Δt=0.7 μs. Due to the Ludwieg tube run duration (~100 ms) and repetition rates of the laser (~15 Hz), single image pairs were obtained per test and multiple runs were required to generate averages and gather fluctuating velocity component statistics from the volume. Based on prior the investigation by Schrijer, 50 nm TiO_2 due to the relaxation time and were dehydrated to avoid agglomeration as suggest by Ragni et al [44]. Figure 15 displays the seeding behind the cylindrical roughness element added on the wedge as well as a representative 3D reconstruction of the vorticity field generated on the wedge. Two pairs of counter rotating vortices are clearly visible and they are likely associated with the horseshoe vortex system that is generated immediately in front the cylinder. Due to the low temporal resolution of the investigation, statistical properties such as the evolution of Reynolds shear stresses or wavenumber spectrums cannot be obtained.

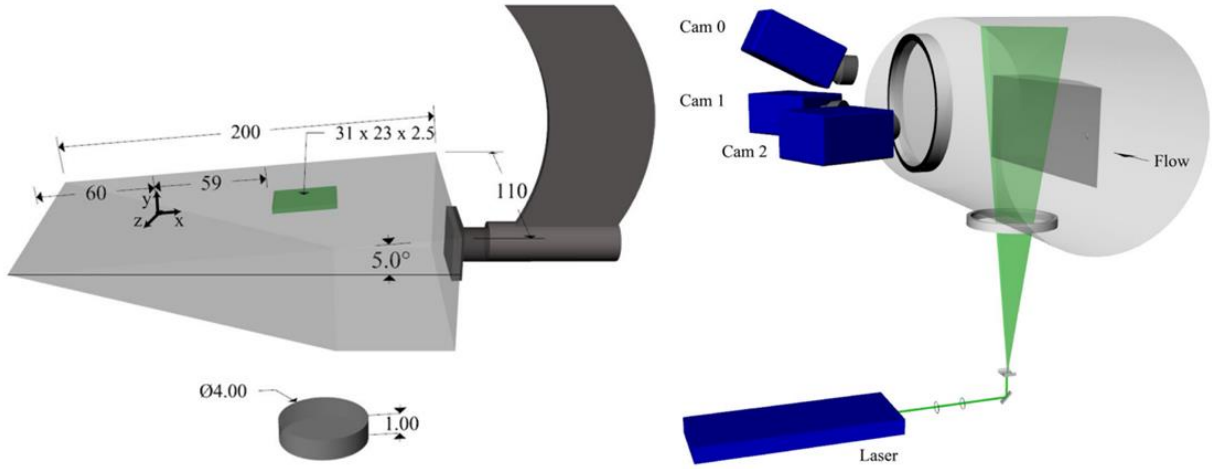

Figure 14 (Left) Sketch of wind tunnel model with cylindrical rougness element placed 60mm from leading edge (Right) Schematic of Tomo-PIV setup. Adapted from [43].

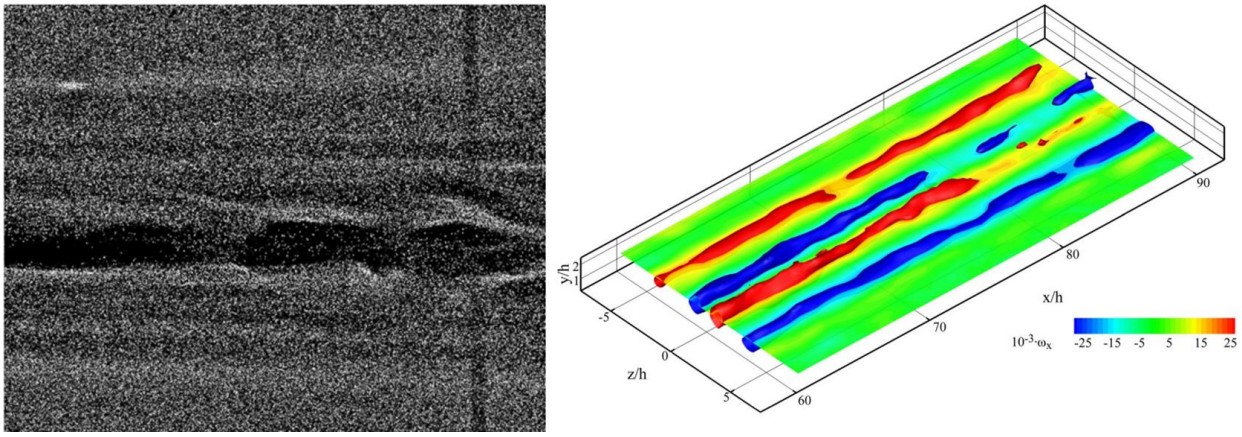

Figure 15 (Left) Post-processed seeding image from the experiment (Right) Stream-wise vorticity with overlaid iso-surfaces of vorticity downstream of cylindrical roughness element. Adapted from [43].

Improvements in laser technology, particularly the advent of burst-mode lasers has allowed for high-power, ultra-high repetition rates enabling techniques such as tomographic PIV at the MHz rates. Zhu et al. demonstrated the first application of burst-mode laser technology for particle image velocimetry of Mach 6 flat plate boundary layer instabilities [45]. The illumination is provided by a Beijing ZK laser, outputting 200mJ/pulse with a pulse width of 10 ns. Three PCO dicam C4 cameras with a 2048 x 2048 pixel sensor were used for the reconstruction of the tomographic volume, each sensor was split into four channels that could operate in double exposure mode to capture each of the PIV pairs. Figure 16 shows the views from each camera used for the tomographic PIV reconstruction. Figure 17 gives the streamwise velocity both in 5 X-Y and X-Z planes taken from the tomographic reconstruction. The wave packets traveling through the unstable boundary layer can be seen in both in the central most plane of both the X-Y and X-Z streamwise velocity. The MHz temporal resolution allows for the instability to be optically tracked, and when compared to wall mounted pressure sensors, the optical tracking of the wave packets allows for accurate estimates of both the frequency and wavelength of the instability.

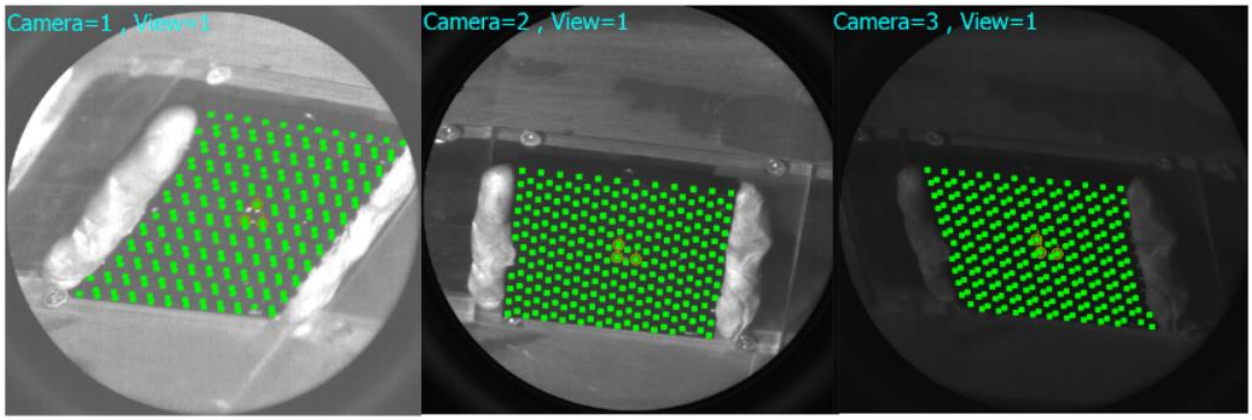

Figure 16 Camera views of a LaVision 058-5 calibration plate for tomographic PIV calibration. Adapted from [45].

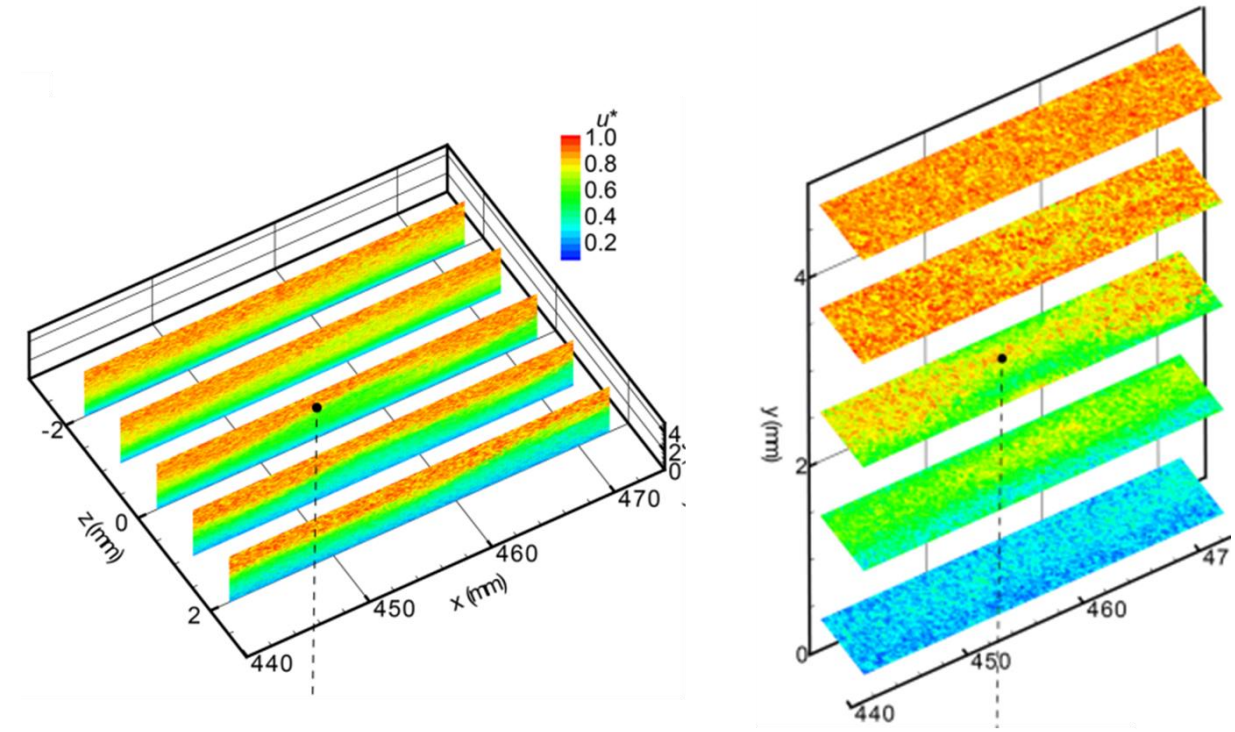

Figure 17 (Left) X-Y Planes of the streamwise velocity component (Right) X-Z planes of the streamwise velocity component. Adapted from [45].

2.2.2 Rayleigh Scattering Visualization

Rayleigh scattering visualization involves the scatter of laser light from particles much smaller than the laser wavelength used as illumination. The present work will focus strictly on the flow visualization method based on Rayleigh scattering light from nm-scale particles of condensate (typically H_2O and CO_2). Particularly when applied to supersonic and hypersonic wind tunnels, a small quantity (typically less than 5% by mass) of a condensable vapor is introduced into the air supply. As the vapor undergoes the nozzle expansion process along with the bulk flow, it condenses into solid-phase clusters, simultaneously, in higher temperature regions such as near walls, shear layers, or across shock waves, the tracer remains gaseous and does not scatter laser light. A laser is focused into a sheet in the wind tunnel test section and the flow is imaged by recording the light scattered from the condensate.

The use of planar laser Rayleigh scatter (PLRS) has recently focused on exploring laminar to turbulent boundary layer transition, as well as shock boundary layer interactions to characterize unstart shock systems. Do et al. used PLRS by seeding CO_2 (25% by volume) to investigate the boundary layer disturbances that precede the formation of an unstart shock system for a rectangular inlet placed in a Mach 5 flow [46]. The starting stagnation pressure and temperature were 350 kPa and 300 K respectively. The importance of the stagnation conditions, particularly low stagnation temperatures to enable phase transition within the tracer will be expanded upon in the experimental section. Laser scatter is achieved using an Nd:YAG laser providing approximately 100 mJ/pulse (at 532 nm) with a repetition rate of 10 Hz. Figure 18 highlights the flow field before and after the inlet undergoes induced unstart via mass injection. It is immediately clear that the turbulent boundary layers present before unstart become largely separated and continue to propagate upstream until reaching the leading edge of the inlet. Additionally, a strong shock emanates from the bottom separated boundary layer, interacting with the original shock wave produced by the inlet cowl. The interaction of these shocks with the boundary layers cause further separation and induce large pressure gradients eventually leading to a full unstart of the inlet.

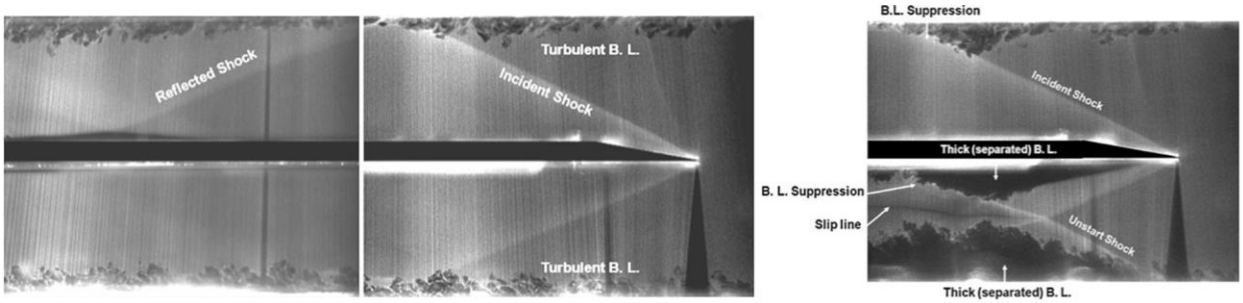

Figure 18 (Left) Started inlet (Right) Inlet undergoing unstart highlighting large scale features. Adapted from [46].

Similarly to particle image velocimetry, advances in laser technology have also enable ultra-high repetition rate PLRS. Zhang and Lee have demonstrated the use of PLRS at an effective repetition rate of 200 kHz to track wave packets and boundary layer instabilities in transitional boundary layers on a flared cone [47-49]. A dual cavity Nd:YAG laser produces two independently controlled pulses with pulse energies of 400 mJ/pulse with a pulse separation of 200 μs. The experiments were performed in the quiet hypersonic wind tunnel at Peking University; Mach 6 flow with a stagnation pressure of 0.71 MPa and a stagnation temperature of 410 K was used to investigate the boundary layer transition. In order to achieve PLRS, approximately 1% by mass of CO_2 was seeded into the flow. Figure 19 highlights the flared cone geometry and two sequential PLRS images taken 5 μs apart. The PLRS images clearly highlight the second mode waves forming prior to a series of the three hairpin packet structures (marked 1-3) resultant from hairpin vortexes that form near the surface. Being able to achieve 5 us pulse separation and produce two sequential PLRS images also allows for optical tracking of the second mode waves present in the boundary layer. The authors found that the second mode travels at approximately 725 m/s, corresponding to about 80% of the free stream velocity, in accordance with the theoretical predictions by Mack [50].

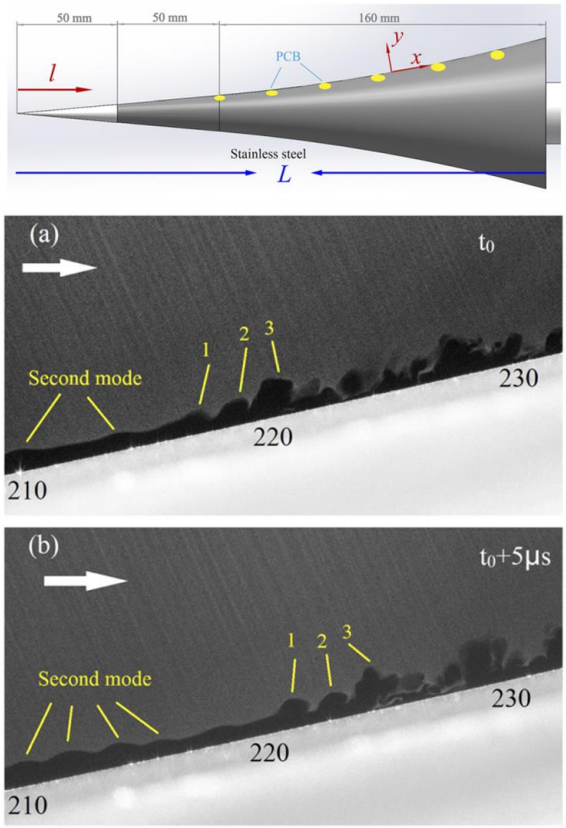

Figure 19 Schematic of the flared cone geometry used for boundary layer transition experiments (a) Transitional boundary layer at t_0 and (b) Boundary layer at t_0 + 5 μs. Adapted from [47].

2.3 Molecular Tagging and Excitation Techniques

2.3.1 Laser Induced Fluorescence

Laser induced fluorescence (LIF), relies on the excitation of an atom or molecule to a higher energy level by the absorption of laser light, followed by the spontaneous emission of light. As a visualization technique, LIF relies on seeding the flow with a tracer or carefully targeting a tracer-species formed for example throughout the combustion process. Table 1 highlights some of the most common species and tracers used for LIF along with their excitation and emission wavelengths. Particularly for supersonic and hypersonic flows, LIF has proven to be a powerful technique both for external aerodynamics and propulsion efforts.

Table 1 Common LIF Tracer Excitation and Emission Wavelengths

Tracer	Excitation Wavelength	Emission Wavelength
Acetone (C_3H_6O)	266 nm	355 nm
Nitric Oxide (NO)	226 nm	235-280 nm
Methylidyne (CH*)	390 nm	430 nm
Hydroxyde (OH)	283nm	310 nm
Formaldehyde (CH_2O)	355 nm	425-485 nm
Toluene (C_7H_8)	266 nm	266-322 nm

Nitric Oxide planar LIF (PLIF) has been used at the NASA Langely Research Center applied to understanding laminar to turbulent boundary layer transition on the heat shield of the NASA Orion Crew Exploration Vehicle (CEV) and the reaction-control-system of a reentry capsule [51, 52]. Similar to the PIV work performed by Avallone et al. a cylindrical roughness element of varying height was used to trip the laminar flow on a wedge model to simulate roughness on the heat shield of the capsule where a turbulent boundary layer can result in a significant increase in heat transfer. Figure 20 (A) highlights the 20° full-angle wedge, the cylindrical element has a diameter of 4 mm and varying heights ranging from 1 mm to 4 mm in 1 mm increments. The cylinder was placed 75 mm downstream from the sharp edge of the wedge. Both a 10 Hz and a 1 MHz laser issuing 226.25 nm light were used to excite the NO and image the boundary layer transition with high spatial resolution at the low speeds and high temporal resolution sacrificing spatial resolution at 1 MHz. UV narrow pass filters with less than 1% transmission at 226 nm and >80% transmission at 235 – 280 nm are used to transmit the LIF signal while rejecting any laser scatter present. Figure 20 (B) and (C) show the influence of the trip on the boundary layer transition, for cylindrical trips 1 mm in height, the seeded gas is deflected approximately 5 diameters while the 4 mm height cylindrical trip deflects the fluid approximately 20 diameters. The plan views such as the one shown in Figure 20 (B) show the sufficient resolution to identify dominant flow structures such as the unsteady wake behind the trop or the vertical structures originating from the horse-shoe vortex wrapping around the front of the cylinder. The MHz rate NO PLIF demonstrated its capability in individually tracking vertical structures in the wake of the trip and can be processed to provide information on the convective velocity of the vortices in the turbulent wake.

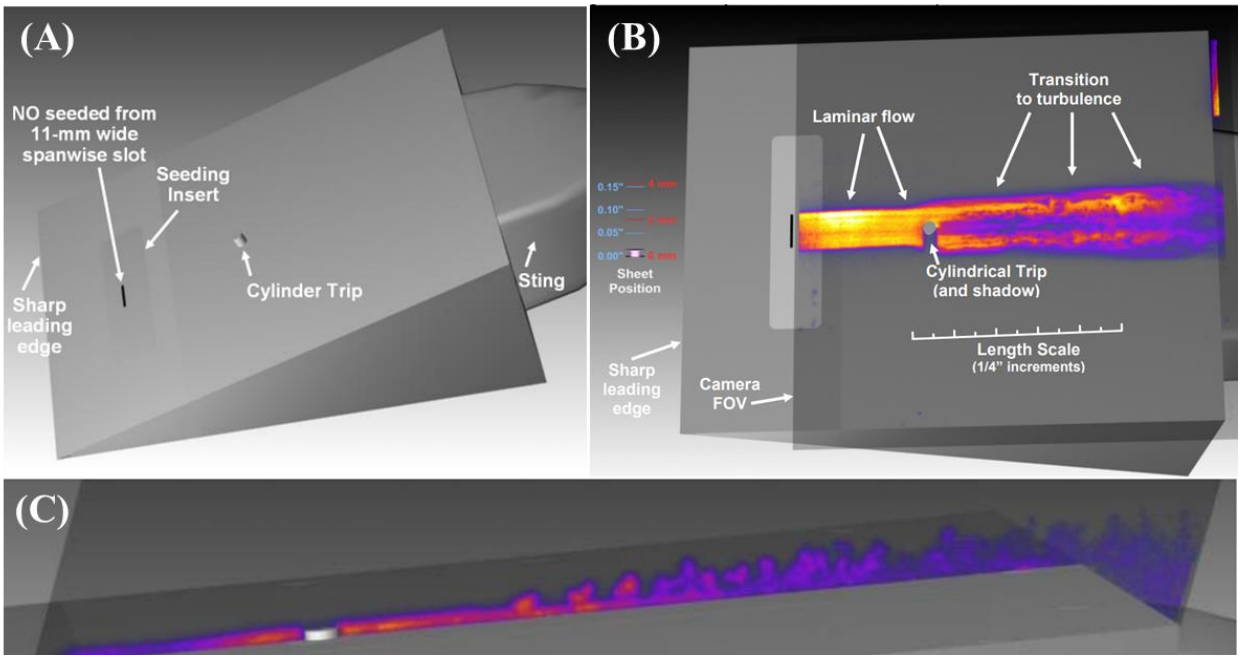

Figure 20 (A) Schematic of wedge used to study boundary layer transition (B) Annotated top view of cylindrical element used to investigate boundary layer transition (C) Lateral view of 1 mm tall cylindrical element causing laminar to turbulent transition. Adapted from [52].

PLIF is also commonly applied to combustion experiments, with recent emphasis on ramjets and scramjets, due to its capability to selectively target the Hydroxyl radical (OH) which is largely regarded as the most accurate representative flame marker [53-55]. Figure 21 highlights the arc-heated combustion test rig (ACT-1) facility developed at the University of Illinois at Urbana-Champaign. ACT-1 produces arc-heated stagnation temperatures ranging from 2000 – 3500 K and typically operates at Mach 4.5, 6, or 9. In order to image the Hydroxyl radical, commonly an excitation wavelength of 283.31 nm is used to provide a strong fluorescence and minimize temperature dependency [56]. In order to achieve this wavelength a Q-switched Nd:YAG laser, operating at 532 nm, is coupled with a dye laser using Rhodamine 590 as the organic dye. Figure 21 also shows an OH PLIF image from the ACT-1 scramjet model operating at Mach 4.5. The hydrogen-air mixture is set to an equivalence ratio of $\varphi = 1.2$. The OH PLIF images reveal that the fuel injector upstream of the cavity does not have a sufficiently large momentum flux ratio to reach the upper surface, thus creating a mixing layer with the incoming air. Additionally, the fuel jet is able to penetrate deep enough to generate a strong turbulent wake capable of sustaining combustion in the wake of the jet. The OH PLIF cross section also reveals that the majority of the unburned fuel occupies the central part of the channel and is enveloped by strong combustion regions along the top and bottom surfaces.

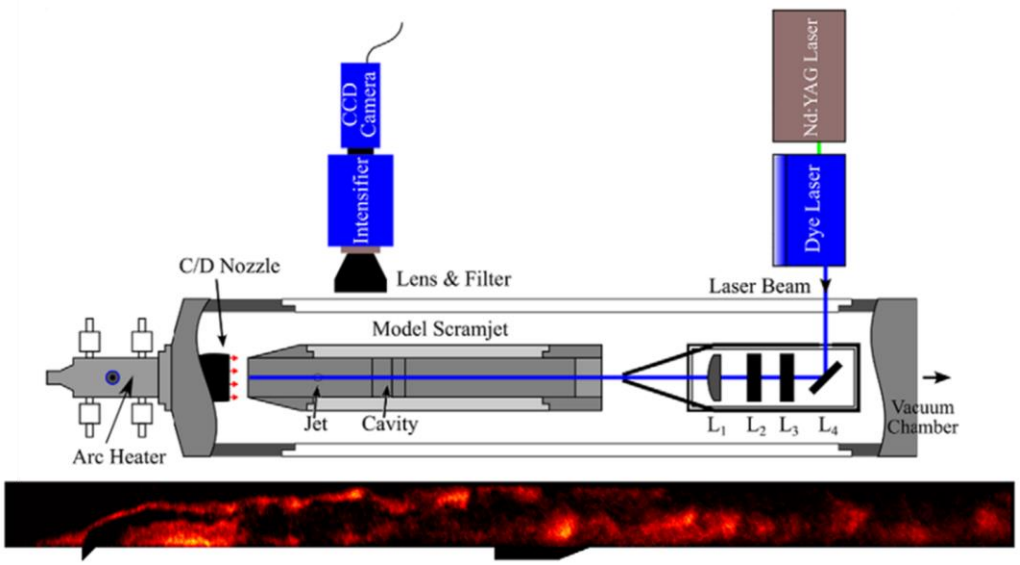

Figure 21 (Top) Facility and PLIF diagnostic schematic of ACT-1 (Bottom) OH PLIF image of scramjet combustor operating at near stoichiometric conditions φ = 1.2. Adapted from [53].

In addition to being a visualization technique, some PLIF imaging can yield quantitative flow field information such as 2D temperature fields. For example, the fluorescence of Toluene (C_7H_8) is correlated with a shift in its emission spectra with increasing temperature. Samper et al. used a two-color PLIF approach, exciting toluene with a 266 nm laser, and imaging two separate wavelengths from the emission spectra, from which the temperature dependence can be estimated [57]. A band-pass filter centered at 280 nm ± 10 nm is used to capture the fluorescence peak and a long-pass filter with a cut off at 280 nm is used to capture the remainder of the fluorescence spectrum. The ratio of the signals from the two filters is then correlated to the temperature calibration of the PLIF signal. Figure 22 shows the two toluene PLIF fluorescence signals as well as the temperature field derived behind the bow shock on a blunt nose cone. The free stream Mach number was 8.9, and as seen from the temperature contour the temperature field on the upper surface of the blunt nose cone could be resolved with the two color PLIF technique, however, near the stagnation region of the blunt nose cone temperature could not properly resolved due to the occurrence of toluene pyrolysis occurring at temperatures over 900 K, the temperature in the stagnation region was estimated to be near T = 1150 K. Toluene PLIF was demonstrated to be reasonably accurate (with estimated temperature uncertainties of 15%) for low-enthalpy facilities, whilst being limited in high-enthalpy configurations due to the pyrolysis limitations above 900 K.

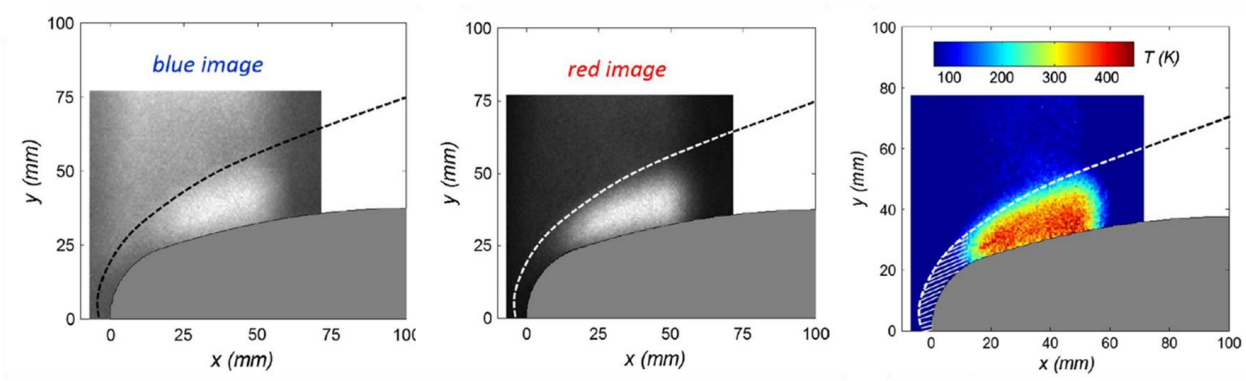

Figure 22 Raw PLIF images with band-pass (blue) and long-pass (red) filters and toluene PLIF temperature contour. Adapted from [57].

2.3.2 Molecular Tagging Approaches

2.3.2.1 Krypton Tagging Velocimetry (KTV)

Krypton tagging velocimetry (KTV) relative to other molecular tagging techniques, relies on a chemically inert tracer and does not significantly alter the local thermodynamic state of the gas through the use of excessive laser energy to generate the molecular excitation. Krypton tagging velocimetry was first demonstrated by Parziale et al. [58] to measure the velocity of an underexpanded jet of N_2/Kr mixtures. The use of metastable krypton as a tracer in a gaseous flow field, relies on tunable pulsed laser to excite and induce the fluorescence of Kr atoms. The excitation and emission strategy for KTV can be summarized as shown in Figure 23. First a "write" tracer line is generate through two-photon excitation using a 214.7 nm laser line. The excitation then decays to resonance states at 819 nm and metastable state at 760.2 nm. The 819 nm transition is imaged by a camera positioned normal to the flow, completing the "write process". The displacement of the tagged metastable krypton is imaged through laser induced fluorescence produced via a laser sheet at 769.5 nm and the spontaneous emission at 829.8 nm also recorded by the camera.

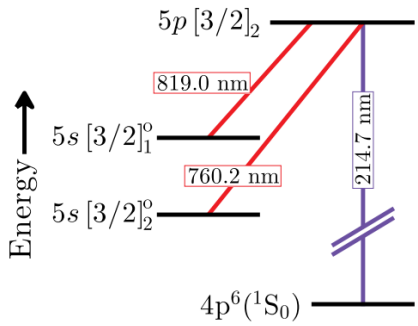

Figure 23 Energy level diagram for KTV. Adapted from [58].

Mustafa et al. demonstrated the ability to perform KTV for large scale hypersonic wind tunnels [59]. The ability to use KTV to measure the free-stream velocity profile of Tunnel 9 at the Arnold Engineering Development Complex (AEDC) was demonstrated for M = 9.4 – 13.2. The read and write sequence described was used to generate and visualized krypton lines. Tunnel 9 typically operates on pure N2, in order to avoid large changes to the thermodynamic state of the gas, a 99% N2 / 1% Kr mixture is used changing the Mach, Reynolds, Prandtl, and Peclet numbers approximately 0.1 – 0.3%. Figure 24 displays an example of the write and read lines from the KTV technique used in Tunnel 9 for a Mach 14 condition with a free stream temperature of 50 K. In order to derive the velocity profile, the two KTV lines imaged 2 μs apart are processed applying a Gaussian peak finding algorithm [60] to find the line centers for each line and estimate the relative displacement between the two. Following, KTV shows to have good agreement throughout the duration of the test as seen from the time series comparison with traditional pressure and temperature measurements used to estimate the velocity in the facility, therefore proving KTV not only yields reasonable results but is also a direct measurement of the velocity field. Furthermore, the maximum deviation of the KTV technique from prior velocity estimates is approximately 2% and is well within the KTV uncertainty.

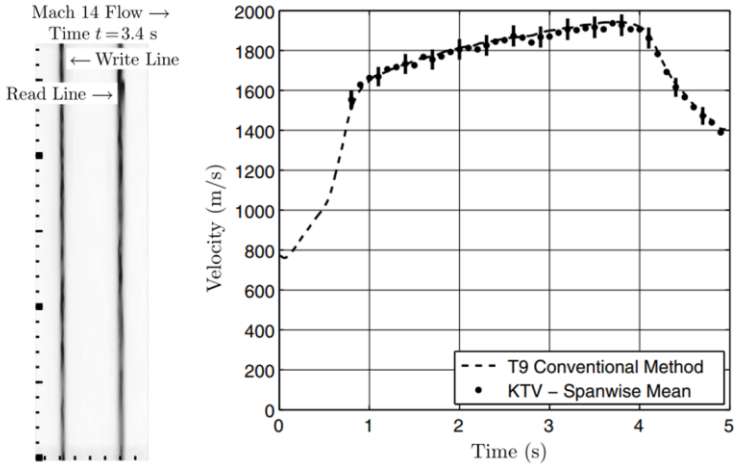

Figure 24 Example of read and write lines for Mach 14 flow and freestreeam velocity from KTV compared to traditional measurements. Adapted from [59].

Further development of the KTV technique has targeted simplifying the read and write process to avoid the use of multiple seed and dye lasers to generate a write line and a secondary laser sheet for the read step. Recent work by Shekhtman et al. has shown that single laser KTV is possible for in air and N_2 flows seeded with 5% and 1% krypton respectively [61]. Instead of the previously described read and write process, krypton atoms are excited with a pulsed-tunable laser to excite the krypton tracer through resonance-enhanced, multiphoton ionization (REMPI). The write step uses two-photon excitation with a 212.6 nm laser. The read step does not require a secondary laser sheet and instead the fluorescence from the residual transition is imaged after a prescribed delay. Relative to the two laser approach, the single laser KTV scheme is simpler and more cost effective with the tradeoff of higher laser energy requirements. Figure 25 shows the single KTV results in N_2 and oxygen doped N_2 flows in a shock tube. The KTV profiles are recorded wall-normal to a hollow sharp-edged cylinder and results are compared to the similarity solution of a compressible, laminar boundary layer. A 10 Hz Nd:YAG coupled with a dye laser is used to produce the 212.6 nm laser line required for the single laser KTV approach, and future work could potentially expand this technique to ultra-fast lasers or tunable burst-mode laser technology.

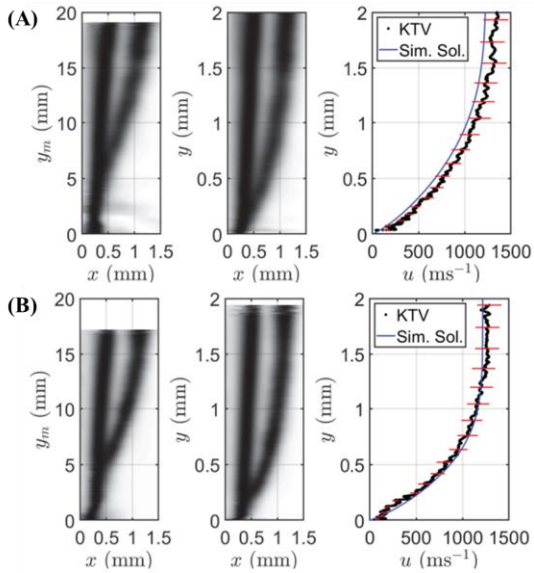

Figure 25 (A) KTV results in 75% N_2 / 20% O_2 and 5% Kr at M=1.7 T=1410 K (B) KTV results in 99% N_2 / 1% Kr at M=1.72 T=1300 K. Adapted from [61].

2.3.2.2 Laser Electronic Excitation Tagging (LEET)

Laser electronic excitation tagging is a nitrogen-fluorescence velocimetry technique that uses femtosecond laser pulses (FLEET) or picosecond laser pulses (PLEET). The principle of the LEET technique is rapid multi-photon excitation of nitrogen with either femtosecond or picosecond lasers, the excitation produces a pool of N atoms from the excited N_2 that undergo recombination and ultimately produce fluorescence. The nitrogen fluorescence produces long-lived signals that can be tracked for velocimetry. Additionally, both FLEET and PLEET only require a laser and a high-speed camera with a gated intensifier. When compared to each the main difference between FLEET and PLEET is that FLEET typically is limited due to laser repetition rates. Zhang et al demonstrated FLEET to measure velocity fields in a Mach 8 nitrogen flow in the wake of a 7° half-angle cone [62]. A 1 KHz Solstice laser with 100 fs pulse width and a wavelength of 800 nm is focused to a point, and the fundamental frequency (800 nm), the second harmonic, and the third harmonic were used to generate the FLEET signal. Figure 26 higlights the experimental setup to obtain the focused laser in the wake of the cone model as well as a comparison between FLEET performed at 800 nm and FLEET performed with the third harmonic (267 nm) of the fundamental laser frequency. The FLEET experiments were performed at a nominal Mach 8 condition with a stagnation temperature of T_o=579 K. The FLEET signal is recorded with a Photron SA-Z camera and a LaVision Intesifier. The 800 nm excitation used 1.8 mJ/pulse while the 267 nm excitation used 0.18 mJ/pulse. It is immediately apparent that the line tagged with 267 nm is a more efficient longer life signal than the one produced at 800 nm. The freestream velocities measured with the PLIF profiles are within 2% of the calculated isentropic velocity.

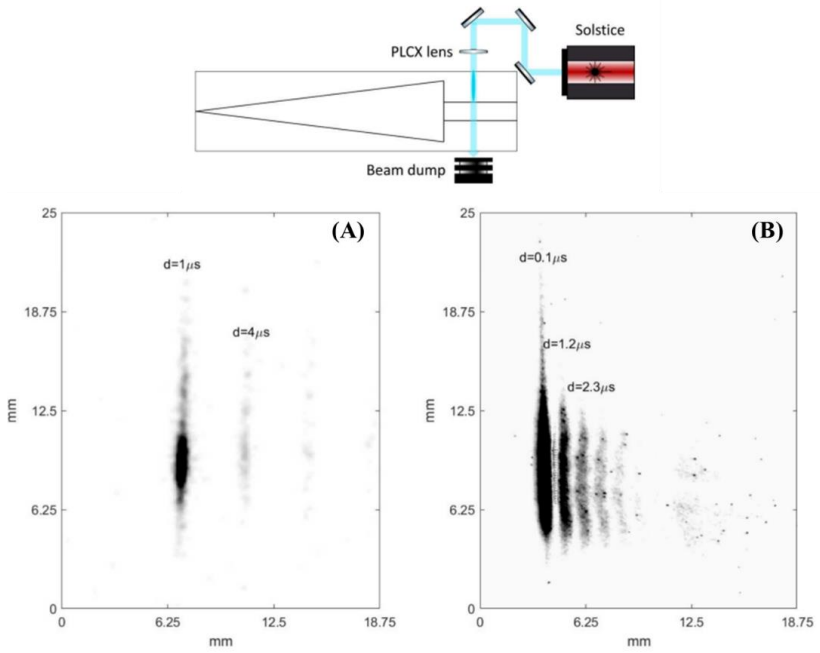

Figure 26 Schematic of FLEET experiment for cone wake velocimetry (A) FLEET at 800 nm excitation (B) FLEET at 267 nm excitation. Adapted from [62].

One of the complications with both FLEET and PLEET diagnostics is that the high intensity of the laser focal points required can lead to surface damage for on body measurements. Hill et al. demonstrated the application of FLEET to measure a hypersonic N_2 boundary layer on an ogive-cylinder model [63]. In order to bypass surface damage to the ogive-cylinder model ports were drilled along the surface to allow the beam strike the interior of the model and act as a beam dump as shown in Figure 27. The FLEET beam was generated using an Astrella Coherent Ti:Sapphire laser operating at 1 kHz with a an average pulse

power of 6 mJ/pulse and a pulse width of 60 fs at 800 nm. In order to image the fluorescence a Photron SA-Z camera with a LaVision two-stage high-speed intensifier. The FLEET experiments were performed in a nitrogen Mach 6 Ludwieg tube at AFRL. Although bypassing the beam provided clear measurements of FLEET velocimetry for near wall flows, care must be given to ablated material being ejected due to surface roughness or machining imperfections that may cause near surface plasma obscuring the FLEET fluorescence.

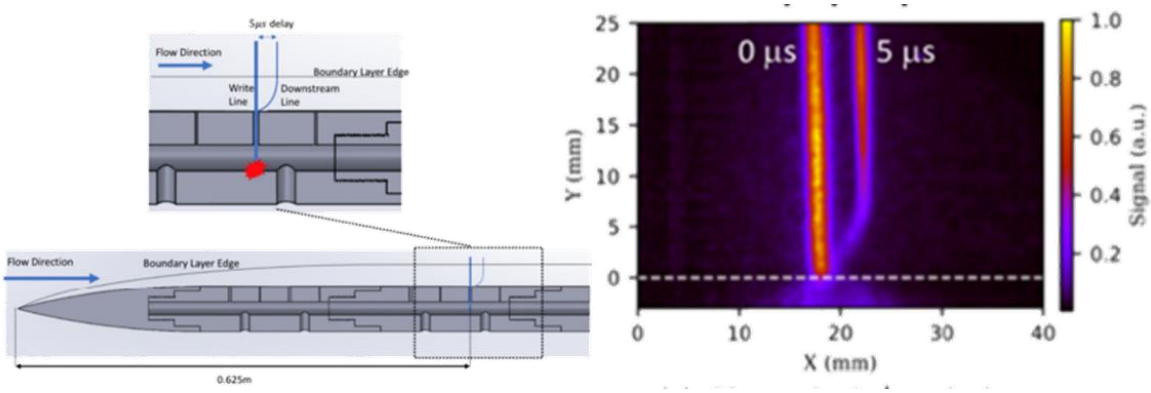

Figure 27 (Left) Schematic of the ogive-cylinder with the ports for bypassing the FLEET beam (Right) Superposition of laser excitation line and fluorescence after 5 μs. Adapted from [63].

Picosecond laser electronic-excitation tagging (PLEET) allows similar measurements at much higher repetition rates due to the advances in burst-mode laser technology enabling high repetition rate, high power, picosecond laser pulses [64, 65]. Hsu et al. demonstrated 100 kHz PLEET also in the Mach 6 Ludwieg tube at AFRL using a 1064 nm, 100 ps pulse width burst-mode laser [64]. Figure 28 highlights the experimental configuration as well as two different PLEET measurements in the freestream of both air and nitrogen flows. It can be noted that the PLEET signal lifetime is much shorter in air when compared to the nitrogen flows. The signal lifetime is approximately 2 μs in air and fluorescence is rapidly quenched by the presence of oxygen. In pure nitrogen flows the fluorescence was able of sustained fluorescence for approximately 20 μs. Compared to FLEET, PLEET enables much higher temporal resolution, but due to the thick plasma lines written, two-dimensional velocimetry becomes much more difficult. In order to overcome these complications shorter laser pulses coupled with higher magnifications must be used.

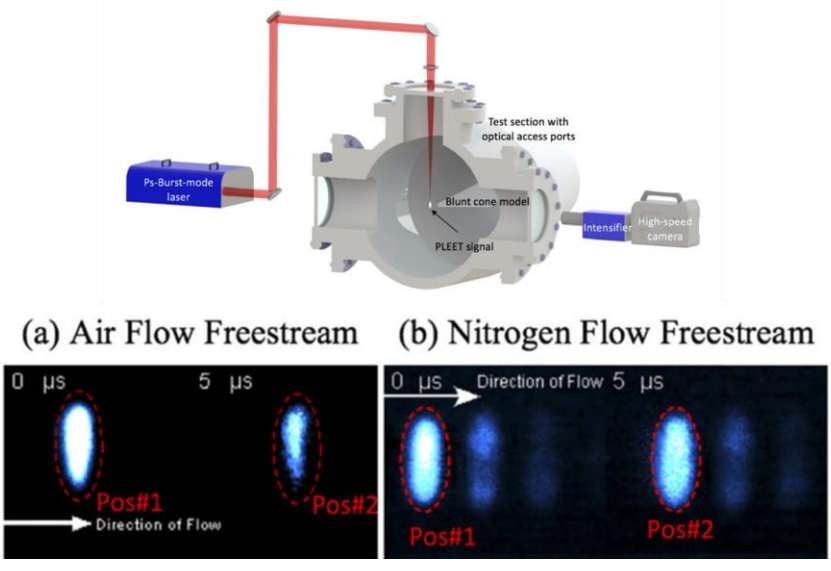

Figure 28 Schematic of PLEET instrumentation and (a) PLEET in air flow (b) PLEET in pure nitrogen flow. Adapted from [64].

.

3. EXPERIMENTS

3.1 Stereoscopic Planar Rayleigh Scatter Visualization

3.1.1 Overview

Rayleigh scattering using CO_2 nano-crystals in particular has been successfully used in the past 25 years to visualize shock flow fields and turbulent boundary layers in wind tunnels. Wu et al. used this method to capture ultra-high speed image sequences of shock-wave/boundary layer interactions in a Mach 2.5 flow field with a bottom wall wedge [66]. Poggie et al. used H_2O and CO_2 Rayleigh scattering to delineate the edge of boundary layers in Mach 3 and Mach 8 flows and provide statistical measurements of large-scale structures in these turbulent layers [67]. More recently, Do et al. used this same technique to study the upstream motion of a shock train and boundary layer separation that characterize the unstart flow field of a Mach 5 wind tunnel [46].

Rayleigh scattering with CO_2 particles has been used to study a variety of compressible flows and shock-boundary layer interactions. However, this technique has been mostly implemented to obtain flow field stream wise views and has not been specifically employed to make flow quality assessments in a wind tunnel facility. The work presented here is motivated by the desire to use this technique to reveal cross-sectional characteristics of the core flow and turbulent boundary layer along the test section of a supersonic wind tunnel. The objective of this study is to characterize the test section flow field to identify possible flow disturbances and non-uniformities. Proper identification of said phenomena can then better inform aerodynamics testing at this wind tunnel facility.

3.1.2 Experimental Setup

The experimental investigation using planar laser CO_2 Rayleigh scattering (PLRS) was performed in the U.S. Naval Academy's (USNA) supersonic blowdown wind tunnel. A representative schematic of this academic facility and its flow path are shown in Figure 29. This wind tunnel features a sliding lower nozzle block which allows variable Mach number operation in the nominal 1.5 – 4.0 range, with a maximum dry-air supply pressure of approximately 1480 kPa (214.7 psia) and a stagnation temperature of 295 K. The tunnel Reynolds number and dynamic pressure operating envelopes are provided in Figure 30.

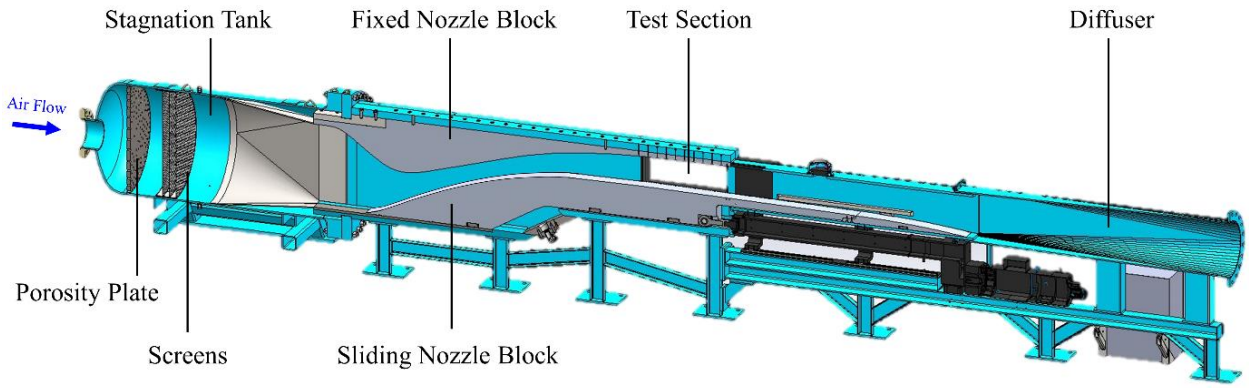

Figure 29 Cross-sectional view of the variable Mach number supersonic wind tunnel facility U.S. Naval Academy.

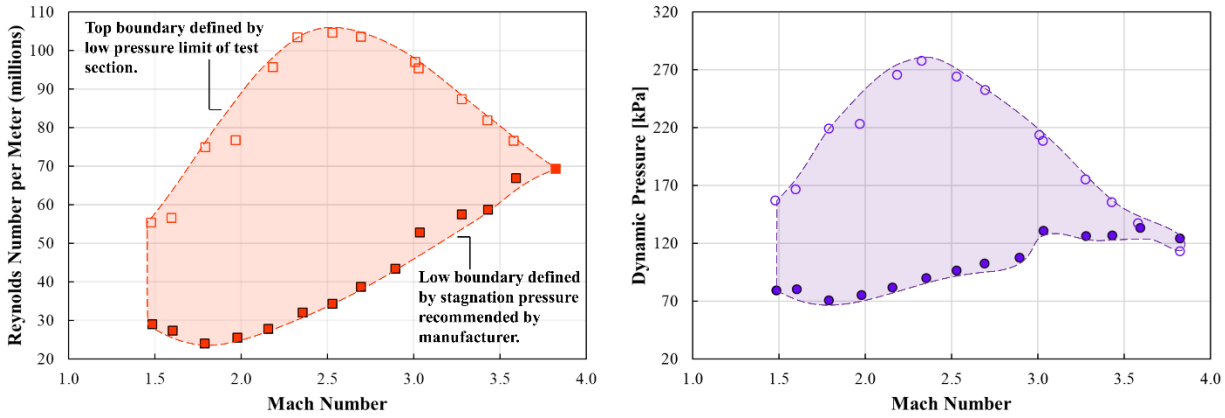

Figure 30 Operational envelope of the U.S. Naval Academy supersonic wind tunnel.

Rayleigh scattering is the scattering of light from particles with sizes smaller than the wavelength of the illumination source [68]. Planar laser Rayleigh scattering of CO_2 requires the crystallization of gaseous CO_2 to generate a fog with nanoscale particles that can scatter light from a laser. This flow visualization technique is most effective in low-temperature and pressure supersonic flows, expanded through the converging/diverging nozzle of a supersonic wind tunnel with low (near-ambient) stagnation temperatures. The expanding nozzle flow experiences both a static pressure and temperature drop and when seeded with gaseous CO_2, undergoes deposition forming solid CO_2 particles. Figure 31 highlights the CO2 sublimation line along with the static temperature and pressure conditions of an isentropically expanded flow for Mach numbers between 1.5 and 4.0. In order for the CO_2 seeded within the air to solidify in this facility, a minimum flow Mach number of 2.0 is needed to reach the pressure and temperature conditions required. The second plot in Figure 31 illustrates the temperature margin for CO_2 nano-crystal sublimation at different flow Mach number conditions. In order to avoid undesired sublimation of CO_2 in the free stream (due to non-ideal nozzle expansion) this study conservatively considered Mach 3.5 and Mach 4.0 test conditions for the experiments. At these flow Mach numbers, the static flow temperature is approximately 80 – 100 K below the CO_2 nano-crystal sublimation temperature.

Injection of gaseous CO_2 into the air supply piping was performed as far upstream as possible to obtain the highest quality images by maximizing CO_2 residence time and mixing. For all the experiments conducted, the amount of CO_2 injected to seed the flow was approximately 1% of the mass flow rate of air, which was about 0.07 kg/s of CO_2 for the range of Mach number conditions tested. A baseline test was performed without any CO_2 seeding to verify light scattering captured in the visualizations was indeed from the CO_2 nano-crystals and not from the condensation of residual moisture in the air supplied to the tunnel.

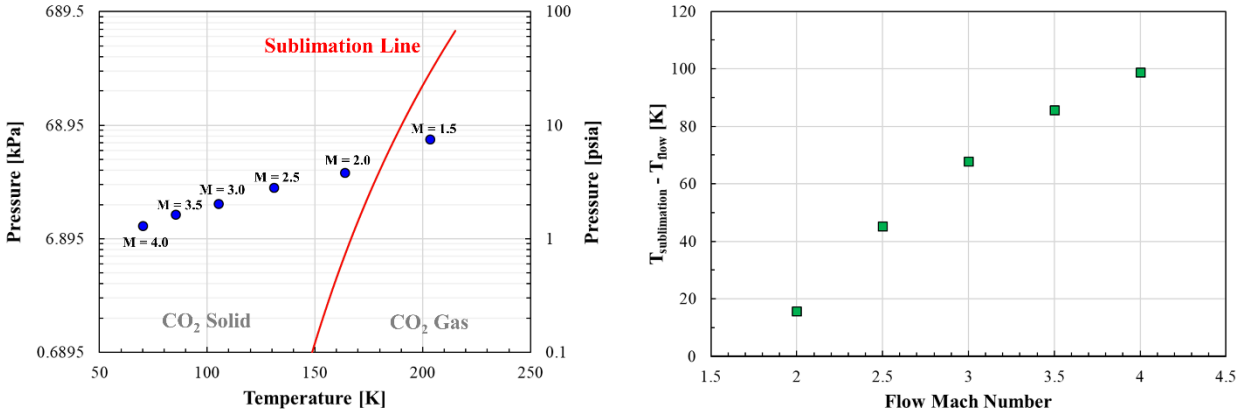

Figure 31 Sublimation line of CO_2 and isentropically expanded flow conditions (left). Temperature margin for CO_2 sublimation as a function of flow Mach number (right).

Flow visualizations of the USNA wind tunnel test section were captured using the CO_2 Rayleigh scattering technique at four stream wise locations. A schematic of the wind tunnel test section in Figure 32 highlights these locations, which are referenced based on their x-coordinate position normalized by the length of the viewing window, L. Note from this schematic that the top nozzle block of the wind tunnel continues to expand through the test section and therefore the height of the flow path increases from the x/L = 0.06 to the x/L = 0.94 location (~6%). Conversely, the bottom nozzle block is nearly flat and the width, W of the test section is constant at 152.4 mm (6 in). Wind tunnel models are typically installed on a sting balance and their leading edge is located between the x/L = 0.77 and x/L = 0.94 planes.

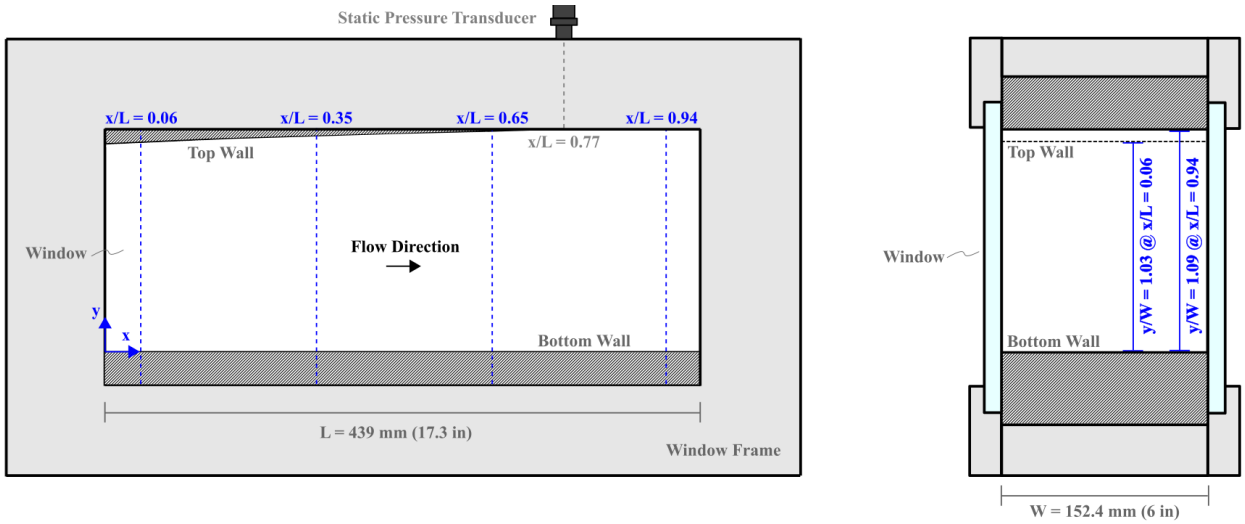

Figure 32 Schematic of the wind tunnel test section showing four normalized stream wise locations investigated (left). Cross-sectional schematic of wind tunnel test section comparing flow path height normalized by test section width (y/W) near inlet and exit, (right).

Top wall static pressure measurements were obtained using a Dwyer Instruments pressure transducer with a 0–345 kPa range located at the x/L = 0.77 position as shown in Figure 32. These measurements together with stagnation pressure measurements obtained in the settling chamber of the wind tunnel were used to determine the actual flow Mach number after the experiments. Table 2 lists these values for the 8 tests performed and compares them against the nominal Mach numbers for the facility, which are the input values entered into the control system before each test to command the lower nozzle block to slide and create the required area ratio. Unless otherwise specified, Mach number conditions referenced in this work refer to the nominal value and not the actual one, which is lower by about 10%. Stagnation conditions recorded and test section Reynolds numbers per meter calculated at the x/L = 0.77 location are also provided in Table 2.

Table 2 Summary of experimental conditions.

x/L	Mach Nominal, M_n	Mach Actual, M_a	Stag. Pressure, P_0	Stag. Temperature, T_0	Reynolds Number, Re/m
-	-	-	*kPa*	*K*	m^{-1}
0.06	3.5	3.2	850.5	299.1	56.0×10^6
	4.0	3.6	1268.0	295.9	70.0×10^6
0.35	3.5	3.2	877.8	298.0	57.8×10^6
	4.0	3.5	1278.3	294.5	71.2×10^6
0.65	3.5	3.2	849.9	297.3	56.3×10^6
	4.0	3.5	1267.1	292.8	71.1×10^6
0.94	3.5	3.2	851.8	300.6	55.2×10^6
	4.0	3.6	1264.4	293.6	70.5×10^6

A LaVision FlowMaster stereoscopic particle image velocimetry (SPIV) system was used to obtain the CO_2 Rayleigh scattering visualizations. The system was comprised of a Quantel Evergreen HP Nd:YAG, dual cavity, pulsed 532 nm laser with a maximum output energy of 380 mJ/pulse, coupled with a pair of high-dynamic-range 5.5 MP Imager sCMOS cameras, placed on each side of the test section. For this study, a single laser head operating at a 10 Hz repetition rate was used to generate the laser sheet. The laser scatter was captured with the laser operating at 66–80% of its maximum output power and the cameras recording at 10 frames per second (fps) coupled with 50 mm f/1.8 Nikon Nikkor lenses. By aiming the cameras at a common calibration target in-situ at the plane of the laser sheet, a perspective calibration was performed, which enabled mapping the raw camera coordinates back into "world" coordinates, effectively de-skewing the image sets. The stereoscopic setup was used to provide the best de-warped image quality possible. Additionally, the highest-contrast image sets for each run condition were selected for processing. Photographs of the LaVision SPIV system setup and the calibration target placed inside the test section of the wind tunnel are shown in Figure 33.

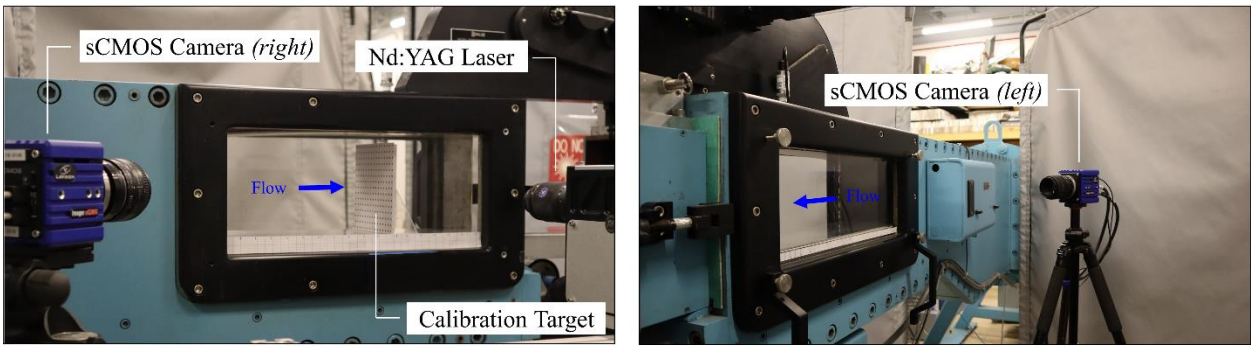

Figure 33 LaVision Stereoscopic PIV system setup using sCMOS cameras, Nd:YAG laser, and calibration target.

The test procedure adopted for the experiments simultaneously initiated the wind tunnel flow, the injection of CO_2, and the LaVision imaging system. This allowed capturing a few images of the flow without any seed particles useful for post-test image processing. Each test was exactly 10 seconds long which provided enough time for the wind tunnel to start (approximately 2 seconds) and the flow of CO_2 through the test section to reach steady state.

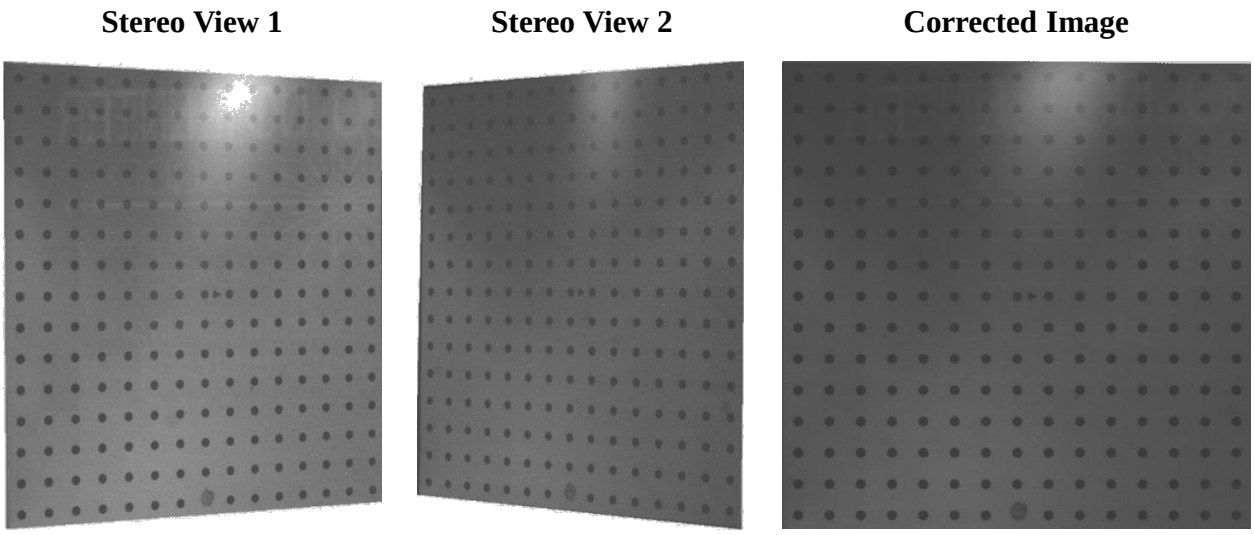

Figure 34 Image de-warping from stereoscopic imaging. First camera perspective (left), second camera perspective (center), reconstructed target (right).

Raw image sets were processed after the experiments to enhance flow features and better visualize the wall boundary layers and flow field in general. First, vibrations present at the camera mounts were corrected using visible reference points in the images. Next, the laser light reflections were reduced and the contrast was enhanced by subtracting an average image from the non-sublimation portion of each image set (nominally the first 1–1.5 sec of data). Then, the test section was masked out using the laser sheet reflections as guidelines. After this, the image sets were de-skewed by applying the perspective calibration(s) to map raw image coordinates (in pixels) into world coordinates (in mm). Lastly, the image sets were averaged for the range when CO_2 sublimation was occurring (i.e., from 3.3–9.9 sec of the time history). Figure 34 shows an example of the reconstruction of the target used for this investigation from the two perspectives taken at the x/L= 0.06 plane.

3.1.3 Comparative Wind Tunnel Flow Simulations

Complementary computational fluid dynamics (CFD) simulations of the flow through the USNA wind tunnel were performed for comparison with the CO_2 visualization data from the Rayleigh scattering experiments. Reynolds-Averaged Navier Stokes (RANS) simulations were performed using a k-ω SST turbulence model for the nominal Mach 3.5 and 4.0 conditions. The flow through this variable Mach number tunnel was modeled following methods similar to the ones used in a previous study for a scaled-up version of this variable-Mach facility by Maxwell et al. [69]. More detailed simulation parameters can be found in prior work by Aguilera et al. [70]. The baseline computational domain with the overlaid structured mesh used for the simulations containing 1.5 million hexahedral elements is shown below in Figure 35.

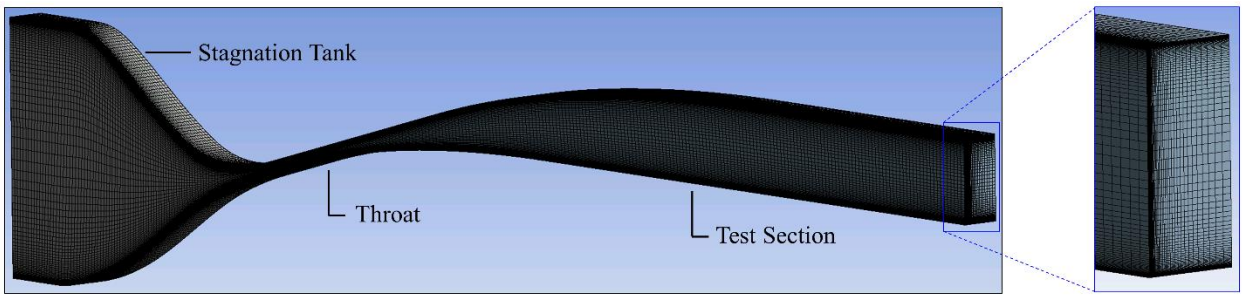

Figure 35 Computational domain of USNA wind tunnel flow path and detailed cross-sectional view of mesh (half-symmetry).

3.1.4 Experimental Results

Sample instantaneous post-processed CO_2 Rayleigh scattering images of the wind tunnel flow obtained at the x/L = 0.94 cross section are presented in Figure 36 for the two nominal Mach number conditions investigated. The field of view corresponds to the full width and height of the test section and the flow direction is into the page. Rayleigh scattering from CO_2 nano-crystals that form in the cold supersonic environment illuminate the core flow, which appears as a large region in the center of the images with a mostly homogenous intensity distribution. At the edges of this cold supersonic region, CO_2 nano-crystals entering the relatively warmer boundary layers sublimate, preventing light scattering from occurring at this interface or further closer to the walls. Dark areas surrounding the core supersonic flow in the images therefore represent regions of the flow with static temperatures above the CO_2 sublimation temperature, which is approximately 175 K for the flow Mach number and pressure conditions of this study. Qualitatively, these dark areas adjacent to the wind tunnel walls can be treated as a general marker of the boundary layer around the test section, but quantitative velocity measurements are necessary to rigorously determine the relationship between the thickness of this dark layer and the velocity boundary layer defined by a 99% free stream velocity threshold.

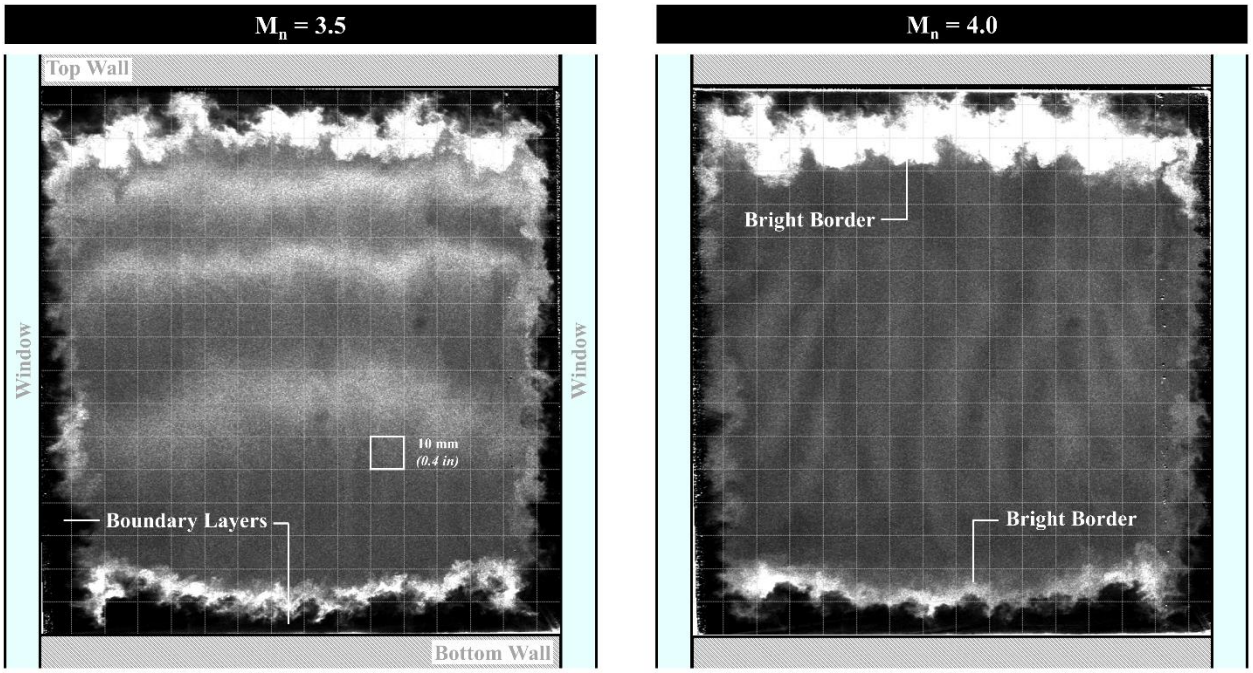

Figure 36 Sample instantaneous CO2 Rayleigh scattering cross-sectional visualizations of nominal Mach 3.5 and Mach 4.0 flows near the exit of the USNA wind tunnel test section (x/L = 0.94).

Representative CO_2 scattering images of the four cross-sectional planes photographed for the nominal Mach 3.5 and Mach 4.0 test conditions in this study are shown in Figure 37. Average images computed using data sets with at least 70 instantaneous images for each test section location are also provided in this figure. Note that the height of the images grows with increasing x/L position as the nozzle continues to expand through the test section as shown previously in Figure 32.

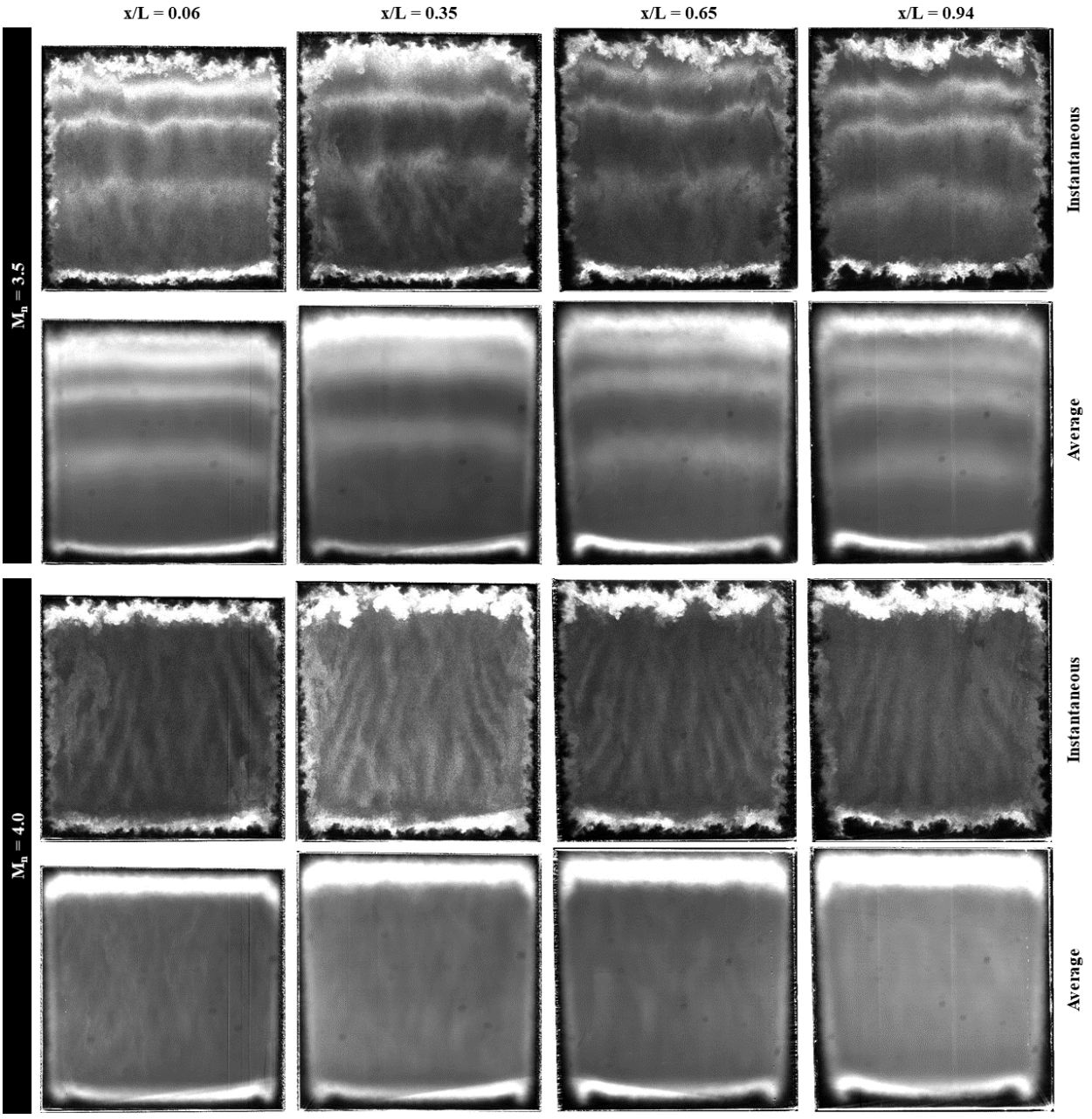

Figure 37 Instantaneous and average cross-sectional images of the USNA wind tunnel test section visualized using a planar laser CO2 Rayleigh scattering technique at four stream wise locations for two different test section nominal Mach numbers.

A careful comparison of the CO_2 Rayleigh scattering images displayed in Figure 37 provides insight into the quality of the supersonic core flow in the wind tunnel and also reveals significant and unexpected differences between the two Mach number conditions tested. For the nominal Mach 3.5 case, the core flow displays distinct bands of increased Rayleigh signal that span the test section horizontally and appear at every stream-wise plane photographed. As shown in the average images, these bright striations are unevenly spaced and appear mostly within the top half of the test section. Interestingly, these features are not visible in any of the images obtained for the nominal Mach 4.0 flow. The core supersonic flow at this higher Mach number has instead a rippled pattern in the vertical direction that is spatially consistent through the test section as seen in the instantaneous images. Average results obtained for this test condition at every x/L location show a fairly uniform distribution of Rayleigh signal with no salient features.

The appearance or absence of horizontal regions with increased brightness in the core flow for the nominal Mach 3.5 and Mach 4.0 conditions can be explained by examining pressure distributions through the wind tunnel flow path from the numerical simulations. Figure 38 and Figure 39 provide side views of the pressure flow field through the supersonic nozzle and the test section along the plane of symmetry for each flow condition. Average Rayleigh scattering cross-sectional images near the inlet (x/L = 0.06) and exit (x/L = 0.94) of the test section are shown adjacent to the corresponding cross-sectional pressure contours from the numerical simulations at those locations.

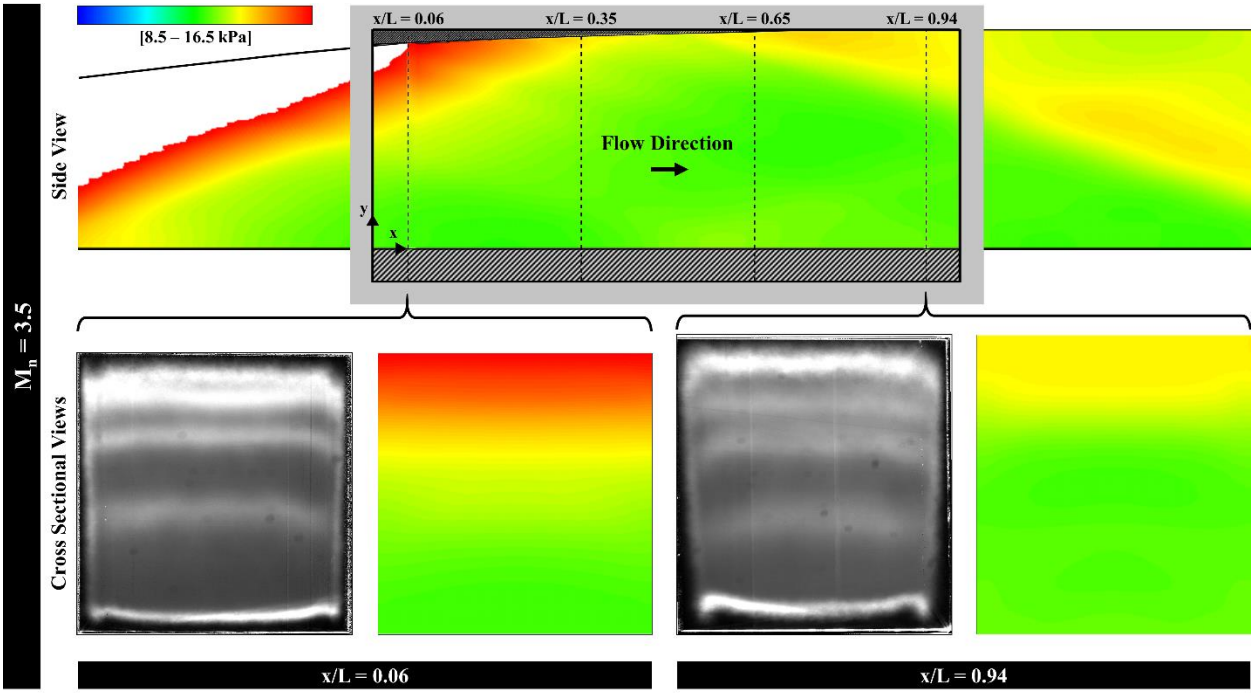

Figure 38 Nominal Mach 3.5 static pressure field through nozzle flow path at center plane from numerical simulations. Comparison of average CO2 Rayleigh scattering images obtained near inlet and outlet of test section with cross- sectional pressure contours at corresponding x/L locations.

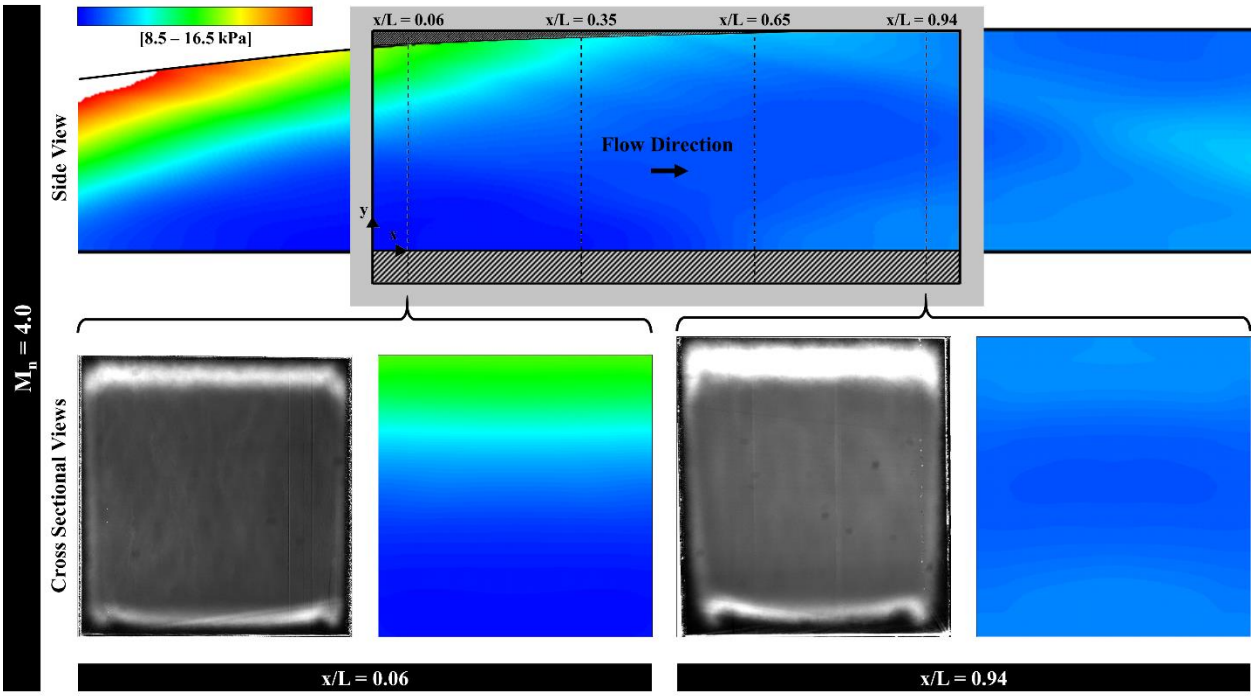

Figure 39 Nominal Mach 4.0 static pressure field through nozzle flow path at center plane from numerical simulations. Comparison of average CO2 Rayleigh scattering images obtained near inlet and outlet of test section with cross-sectional pressure contours at corresponding x/L locations.

A discernible characteristic of the flow path boundary layers shown in Figure 37 is their asymmetric thickness around the test section. In general, boundary layers along top and bottom walls appear to be much thicker in comparison to those along the side walls. Using the instantaneous image for the nominal Mach 3.5 test condition in Figure 36 as an example, the thickness of the boundary layer along the test section floor can be up to 12% of the test section height at the x/L = 0.94 location, while the thinnest part of the side wall boundary layer is approximately a quarter of that value near the top wall. Similarly, inspection of the turbulent flow structures in the boundary layers indicate that the top and bottom walls are populated with large-scale structures which are not apparent along the side walls.

Interactions between expansion fans and turbulent wall boundary layers promote growth of the boundary layer thickness and an increase in size of large-scale structures downstream of the interaction [71, 72]. Differences in the boundary layer thickness and turbulent structure topology between side walls and top/bottom surfaces can be attributed to the expansion flow field in the wind tunnel where wave reflections are observed throughout the test section. These wave interactions and their effect on turbulence may also be responsible for the significant increase in Rayleigh scattering signal observed in Figure 36 along the outer edge of the floor and ceiling boundary layers. These bright borders are regions of strong turbulent mixing and shear where the static temperature is not high enough to trigger CO_2 nano-crystal sublimation and the induced vorticity increases laser scattering.

Thickening of side wall boundary layers from top to bottom of the test section can be seen from the Rayleigh scattering visualizations. Figure 40 highlights this phenomenon by comparing vertical sections of instantaneous and average Rayleigh scattering images at the most downstream cross-sectional plane. From these images, the bottom part of the boundary layer near the test section wall is at least twice as thick as the top part near the ceiling for both Mach number conditions. Corresponding Mach number contours at the x/L = 0.94 location are also provided in Figure 40 for comparison and numerical modeling validation.

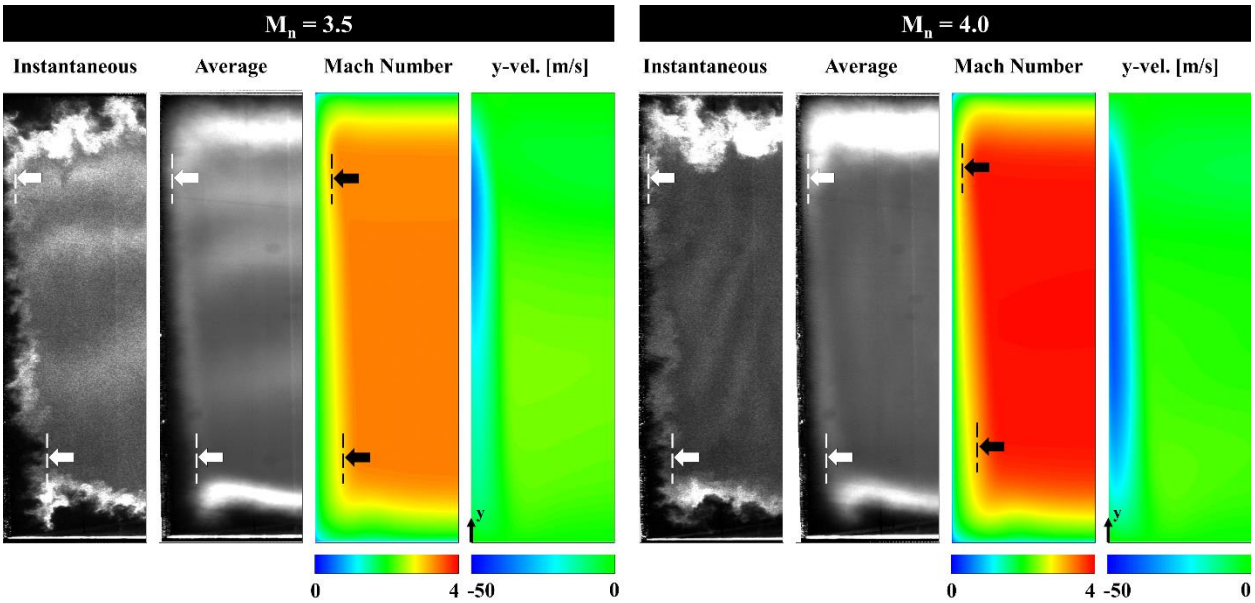

Figure 40 Thickening of side wall boundary layers observed in Rayleigh scattering flow visualizations and Mach number contours from numerical simulations.

The underlying physical mechanism responsible for the thickening of the boundary layers along the wind tunnel side walls is associated with the flow expansion and uneven pressure distribution that occurs through the supersonic nozzle as explained by Sabnis et al. [73]. To illustrate this point, consider the sample Mach number contours along the center plane of the USNA supersonic nozzle presented in Figure 41. Line segment AB represents the last flow characteristic of the expansion and connects two points in the flow where the Mach number is the same. From this characteristic, note that the flow reaches full expansion at point A upstream of point B. As a result, at any given axial location between these two points the stream wise velocity near the tunnel floor is higher than near the tunnel ceiling. This causes a vertical pressure imbalance which is clearly visible in the cross-sectional pressure contours presented earlier in Figure 38 and Figure 39. This pressure gradient induces a vertical secondary flow with a magnitude in the order of 4-8% of the free stream velocity which drags side wall boundary layer fluid downward, making the boundary layer thin at the top and thick at the bottom. Vertical velocity contours obtained from the numerical simulations in this study are presented in Figure 40 for both nominal Mach numbers at the x/L = 0.94 plane illustrating the location and magnitude of this secondary flow near the test section side wall.

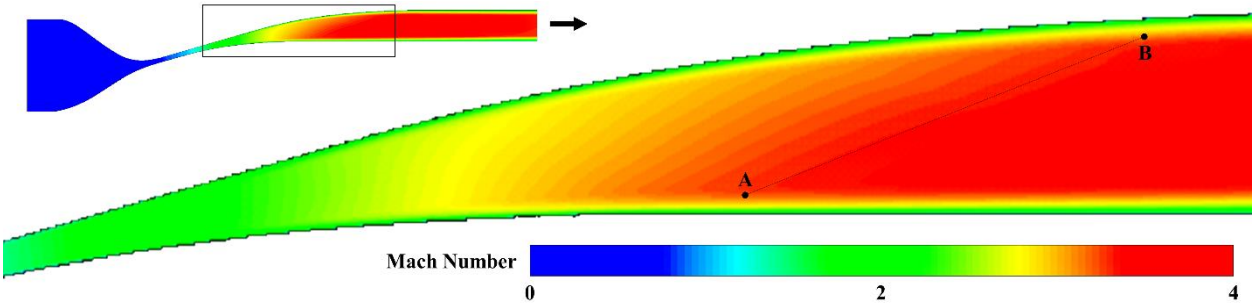

Figure 41 Mach number contours along symmetry plane of the USNA wind tunnel nozzle to illustrate the origin of stream wise velocity non-uniformity and pressure gradients in the test section.

A final noticeable result from the average Rayleigh scattering images presented in Figure 37 is the presence of two symmetric lobes in the floor boundary layer near the side walls of the test section. Figure 42 provides close up views of these features visible in the instantaneous images but more readily seen in the average results for both test conditions.

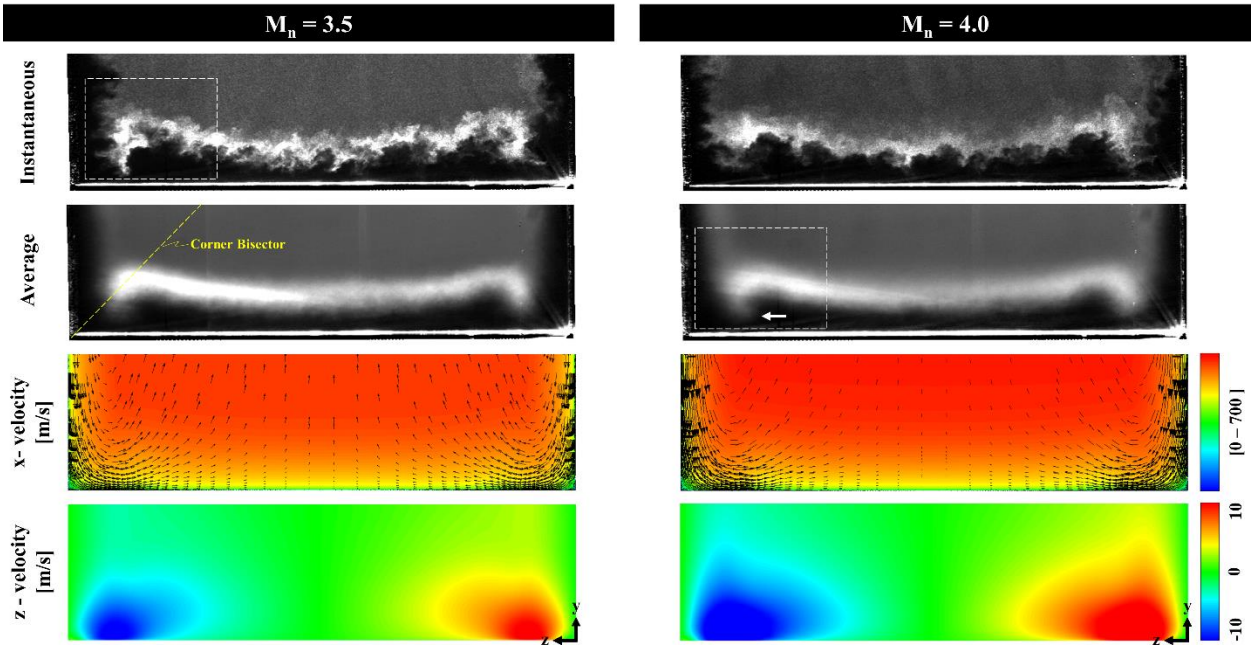

Figure 42 Close-up views of bottom wall boundary layer lobes observed near test section corners in both instantaneous and average CO2 Rayleigh scattering visualizations. Comparison against stream-wise velocity contours with overlaid in-plane velocity vectors and contours of z-velocity from numerical simulations.

Researchers have investigated supersonic turbulent flows in rectangular ducts and proposed the existence of counter-rotating vortex pairs in the corners, one along the side wall and one along the top/bottom wall [74-76]. In the absence of secondary vertical flows within the duct, these counter-rotating vortices transport high momentum fluid from the core supersonic flow into the corner boundary layer, generating a symmetric flow field along the corner bisector [76]. In the presence of vertical secondary flows such as the ones described earlier for the USNA wind tunnel, this symmetric corner flow field is significantly altered. As seen in the average images provided in Figure 42, some Rayleigh signal is detected in regions deep into the boundary layer adjacent to the two lobes, but this fluid is entrained into the bottom wall boundary layer exclusively and not into the corner. Contours of stream wise velocity with in-plane velocity vectors from the numerical simulations suggest that the vertical secondary flow plays an important role in the complex corner flow field seen in the visualizations.

As shown by the in-plane velocity vectors in Figure 42, the vertical flow near the wall travels downward but curls as it approaches the bottom wall. Core fluid entrained by this motion is therefore injected into the bottom wall boundary but away from the corner. Contours of z-velocity shown in Figure 42 indicate that very near the bottom wall, there is a low magnitude velocity component towards the center of the cross section. This result suggests that core fluid transported into the floor boundary layer can also end up partially rolling underneath it as indicated by a white arrow in the nominal Mach 4.0 average image. In doing so, the floor boundary layer is lifted locally, which gives rise to the lobes observed.

4. CONCLUSION

An experimental characterization of the flow quality in the USNA blowdown supersonic wind tunnel was conducted using planar CO_2 Rayleigh scattering visualization. Cross-sectional views of the flow were obtained at four stream wise locations that spanned the length of the test section. Nominal Mach 3.5 and 4.0 flows were selected for the experiments to avoid undesired CO_2 sublimation in the free stream. Supersonic core flow and turbulent boundary layer characteristics were specifically examined from the visualizations.

Image regions adjacent to the flow path walls and devoid of Rayleigh signal were used as a qualitative marker for test section boundary layers in the test section. Overall, boundary layers for both Mach number conditions appeared to be very similar and grew from test section inlet to outlet. However, individual examination of ceiling, floor, and side wall boundary layers revealed appreciable differences in their characteristics. Boundary layers along the side walls appeared to be significantly thinner and had less distinct large scale structures in comparison to boundary layers along top and bottom walls. Side wall boundary layers were thinnest near the ceiling and thickest near the test section floor. Bottom wall boundary layers had two distinct lobe features near the test section corners with clear entrainment of cold core fluid. The origin of these specific boundary layer characteristics was linked to uneven expansion through the nozzle driving a pressure gradient along the height of the tunnel, inducing secondary vertical flows along the side walls.

Finally, a few comments can be provided on flow quality and implications of the results for future aerodynamics testing at the USNA facility:

1) Expansion fans and weak pressure waves reflecting through the test section are undesirable if impingement of these acoustic disturbances on a test model cause boundary layer separation and spurious measurements. Based on the results presented in this study, wind tunnel testing at a nominal Mach 4.0 condition appears to be preferable in comparison to the nominal Mach 3.5 because the flow expansion at this higher Mach number generates a more uniform flow field near the exit of the test section where the leading edge of a wind tunnel model is typically found.

2) The useful supersonic core is biased towards the top of the test section due to the thickening of side wall boundary layers near the test section floor and corner effects evidenced along the bottom of the test section. Most sting mounted models tested at the USNA wind tunnel are located near the center of the test section, but any future test that would require placing a model closer to the bottom floor should take into consideration that the boundary layer can be much large depending on positioning and a model at that location could be more susceptible to acoustic noise radiated from the side wall boundary layers.

3) Wind tunnel models installed upstream of the $x/L = 0.94$ plane should consider that the flow quality degrades closer to the inlet of the test section where the effect of the flow expansion on flow non-uniformity is worse.

REFERENCES

1. Miles, R.B., *Optical diagnostics for high-speed flows.* Progress in Aerospace Sciences, 2015. **72**: p. 30-36.
2. Krehl, P.O., *History of shock waves, explosions and impact: a chronological and biographical reference*. 2008: Springer Science & Business Media.
3. Maguire, B.L., E.P. Muntz, and J.R. Mallin, *Visualization technique for low-density flow fields.* IEEE Transactions on Aerospace and Electronic Systems, 1967(2): p. 321-326.
4. Trolinger, J., W. Farmer, and R. Belz, *Multiple exposure holography of time varying three-dimensional fields.* Applied optics, 1968. **7**(8): p. 1640-1641.
5. Havener, A.G. and R.J. Radley Jr, *Turbulent Boundary-Layer Flow Separation Measurements Using Holographic Interferometry.* AIAA Journal, 1974. **12**(8): p. 1071-1075.
6. Schäfer, F.P., W. Schmidt, and J. Volze, *Organic dye solution laser.* Applied Physics Letters, 1966. **9**(8): p. 306-309.
7. Sorokin, P.P. and J. Lankard, *Stimulated emission observed from an organic dye, chloro-aluminum phthalocyanine.* IBM Journal of Research and Development, 1966. **10**(2): p. 162-163.
8. Miles, R.B., *Resonant doppler velocimeter.* The Physics of Fluids, 1975. **18**(6): p. 751-752.
9. Zimmermann, M. and R. Miles, *Hypersonic-helium-flow-field measurements with the resonant Doppler velocimeter.* Applied Physics Letters, 1980. **37**(10): p. 885-887.
10. McDaniel, J.C., B. Hiller, and R.K. Hanson, *Simultaneous multiple-point velocity measurements using laser-induced iodine fluorescence.* Optics Letters, 1983. **8**(1): p. 51-53.
11. Paul, P.H., M. Lee, and R. Hanson, *Molecular velocity imaging of supersonic flows using pulsed planar laser-induced fluorescence of NO.* Optics Letters, 1989. **14**(9): p. 417-419.
12. Lozano, A., B. Yip, and R.K. Hanson, *Acetone - a Tracer for Concentration Measurements in Gaseous Flows by Planar Laser-Induced Fluorescence.* Experiments in Fluids, 1992. **13**(6): p. 369-376.
13. Huber-Wälchli, P. and J.W. Nibler, *CARS spectroscopy of molecules in supersonic free jets.* The Journal of Chemical Physics, 1982. **76**(1): p. 273-284.
14. Cummings, E., *Laser-induced thermal acoustics: simple accurate gas measurements.* Optics letters, 1994. **19**(17): p. 1361-1363.
15. Koochesfahani, M. *Molecular Tagging Velocimetry (MTV)-progress and applications*. in *30th Fluid Dynamics Conference*. 1999.
16. Eckbreth, A.C. and T.J. Anderson, *Dual broadband CARS for simultaneous, multiple species measurements.* Applied optics, 1985. **24**(16): p. 2731-2736.
17. Miles, R., et al., *Instantaneous profiles and turbulence statistics of supersonic free shear layers by Raman excitation plus laser-induced electronic fluorescence (RELIEF) velocity tagging of oxygen.* Experiments in fluids, 1989. **8**(1-2): p. 17-24.
18. Pitz, R.W., et al., *Unseeded velocity measurement by ozone tagging velocimetry.* Optics letters, 1996. **21**(10): p. 755-757.
19. Hiller, B., et al., *Velocity visualization in gas flows using laser-induced phosphorescence of biacetyl.* Review of Scientific Instruments, 1984. **55**(12): p. 1964-1967.
20. Boedeker, L.R., *Velocity measurement by H 2 O photolysis and laser-induced fluorescence of OH.* Optics letters, 1989. **14**(10): p. 473-475.
21. Durst, F., A. Melling, and J.H. Whitelaw, *Principles and practice of laser-Doppler anemometry.* NASA STI/Recon Technical Report A, 1976. **76**: p. 47019.
22. Adrian, R.J., *Particle-imaging techniques for experimental fluid mechanics.* Annual review of fluid mechanics, 1991. **23**(1): p. 261-304.
23. Westerweel, J., *Fundamentals of digital particle image velocimetry.* Measurement science and technology, 1997. **8**(12): p. 1379.
24. Settles, G.S., *Schlieren and shadowgraph techniques: visualizing phenomena in transparent media*. 2001: Springer Science & Business Media.

25. Settles, G.S. and M.J. Hargather, *A review of recent developments in schlieren and shadowgraph techniques.* Measurement Science and Technology, 2017. **28**(4): p. 042001.
26. Krehl, P. and S. Engemann, *August toepler—the first who visualized shock waves.* Shock Waves, 1995. **5**(1): p. 1-18.
27. Laurence, S., et al., *Time-resolved visualization of instability waves in a hypersonic boundary layer.* AIAA journal, 2012. **50**(1): p. 243-246.
28. Laurence, S., A. Wagner, and K. Hannemann, *Schlieren-based techniques for investigating instability development and transition in a hypersonic boundary layer.* Experiments in Fluids, 2014. **55**(8): p. 1-17.
29. Martin, N., et al. *Implementation of a laser-based schlieren system for boundary layer instability investigation in the VKI H3 hypersonic wind tunnel*. in *AIAA Scitech 2019 Forum*. 2019.
30. Casper, K.M., et al. *Simultaneous pressure measurements and high-speed schlieren imaging of disturbances in a transitional hypersonic boundary layer*. in *43rd AIAA Fluid Dynamics Conference*. 2013.
31. Raffel, M., *Background-oriented schlieren (BOS) techniques.* Experiments in Fluids, 2015. **56**(3): p. 1-17.
32. Heineck, J.T., et al., *Background-Oriented Schlieren Imaging of Supersonic Aircraft in Flight.* AIAA Journal, 2021. **59**(1): p. 11-21.
33. Fisher, T., M.K. Quinn, and K. Smith, *An experimental sensitivity comparison of the schlieren and background-oriented schlieren techniques applied to hypersonic flow.* Measurement Science and Technology, 2019. **30**(6): p. 065202.
34. Weinstein, L.M., *Large-field high-brightness focusing schlieren system.* AIAA journal, 1993. **31**(7): p. 1250-1255.
35. VanDercreek, C., M. Smith, and K. Yu. *Focused schlieren and deflectometry at AEDC hypervelocity wind tunnel No. 9*. in *27th AIAA Aerodynamic Measurement Technology and Ground Testing Conference*. 2010.
36. VanDercreek, C.P., *Hypersonic application of focused schlieren and deflectometry*. 2010: University of Maryland, College Park.
37. Raffel, M., C.E. Willert, and J. Kompenhans, *Particle image velocimetry: a practical guide*. Vol. 2. 1998: Springer.
38. Melling, A., *Tracer particles and seeding for particle image velocimetry.* Measurement science and technology, 1997. **8**(12): p. 1406.
39. Stokes, G.G., *On the effect of the internal friction of fluids on the motion of pendulums.* 1851.
40. Henderson, C.B., *Drag coefficients of spheres in continuum and rarefied flows.* AIAA journal, 1976. **14**(6): p. 707-708.
41. Loth, E., *Compressibility and rarefaction effects on drag of a spherical particle.* AIAA journal, 2008. **46**(9): p. 2219-2228.
42. Schrijer, F., F. Scarano, and B. Van Oudheusden, *Application of PIV in a Mach 7 double-ramp flow.* Experiments in fluids, 2006. **41**(2): p. 353-363.
43. Avallone, F., et al., *Tomographic PIV investigation of roughness-induced transition in a hypersonic boundary layer.* Experiments in fluids, 2014. **55**(11): p. 1-12.
44. Ragni, D., et al., *Particle tracer response across shocks measured by PIV.* Experiments in Fluids, 2011. **50**(1): p. 53-64.
45. Zhu, Y., H. Yuan, and C. Lee, *Ultrafast tomographic particle image velocimetry investigation on hypersonic boundary layers.* Physics of Fluids, 2020. **32**(9): p. 094103.
46. Do, H., et al., *Visualizing supersonic inlet duct unstart using planar laser Rayleigh scattering.* Experiments in fluids, 2011. **50**(6): p. 1651-1657.
47. Zhang, C., *Evolution of the second mode in a hypersonic boundary layer.* Physics of Fluids, 2020. **32**(12): p. 121706.
48. Zhang, C. and C. Lee, *Rayleigh-scattering visualization of the development of second-mode waves.* Journal of Visualization, 2017. **20**(1): p. 7-12.

49. Zhang, C., et al., *Transition in hypersonic boundary layers.* AIP Advances, 2015. **5**(10): p. 107137.
50. Mack, L.M., *Boundary-layer linear stability theory*. 1984, California Inst of Tech Pasadena Jet Propulsion Lab.
51. Combs, C., et al. *NO PLIF Visualizations of the Orion Capsule in LENS-I*. in *51st AIAA Aerospace Sciences Meeting including the New Horizons Forum and Aerospace Exposition*. 2013.
52. Danehy, P., et al. *High-speed PLIF imaging of hypersonic transition over discrete cylindrical roughness*. in *48th AIAA Aerospace Sciences Meeting Including the New Horizons Forum and Aerospace Exposition*. 2010.
53. Baccarella, D., et al., *Development and testing of the ACT-1 experimental facility for hypersonic combustion research.* Measurement Science and Technology, 2016. **27**(4): p. 045902.
54. Boyce, R., N. Mudford, and J. McGuire, *OH-PLIF visualisation of radical farming supersonic combustion flows.* Shock Waves, 2012. **22**(1): p. 9-21.
55. Johansen, C.T., et al., *OH PLIF visualization of the UVa supersonic combustion experiment: configuration A.* Journal of Visualization, 2014. **17**(2): p. 131-141.
56. Ben-Yakar, A. and R. Hanson. *Hypervelocity combustion studies using simultaneous OH-PLIF and schlieren imaging in an expansion tube*. in *35th joint propulsion conference and exhibit*. 1999.
57. Estruch-Samper, D., et al., *Toluene-based planar laser-induced fluorescence imaging of temperature in hypersonic flows.* Experiments in Fluids, 2015. **56**(6): p. 1-13.
58. Parziale, N., M. Smith, and E. Marineau, *Krypton tagging velocimetry of an underexpanded jet.* Applied optics, 2015. **54**(16): p. 5094-5101.
59. Mustafa, M., et al., *Nonintrusive freestream velocity measurement in a large-scale hypersonic wind tunnel.* AIAA journal, 2017: p. 3611-3616.
60. O'Haver, T., *A pragmatic introduction to signal processing.* University of Maryland at College Park, 1997.
61. Mustafa, M.A., D. Shekhtman, and N.J. Parziale. *Single-Laser Krypton Tagging Velocimetry (KTV) Investigation of Air and N2 Boundary-Layer Flows Over a Hollow Cylinder in the Stevens Shock Tube*. in *AIAA Scitech 2019 Forum*. 2019.
62. Zhang, Y., et al. *Hypersonic wake measurements behind a slender cone using FLEET velocimetry*. in *AIAA Aviation 2019 Forum*. 2019.
63. Hill, J.L., et al., *Hypersonic N 2 boundary layer flow velocity profile measurements using FLEET.* Applied Optics, 2021. **60**(15): p. C38-C46.
64. Hsu, P.S., et al., *100 kHz PLEET velocimetry in a Mach-6 Ludwieg tube.* Optics Express, 2020. **28**(15): p. 21982-21992.
65. Jiang, N., et al., *Seedless velocimetry at 100 kHz with picosecond-laser electronic-excitation tagging.* Optics letters, 2017. **42**(2): p. 239-242.
66. Wu, P., W.L. Lempert, and R.B. Miles, *Megahertz pulse-burst laser and visualization of shock-wave/boundary-layer interaction.* AIAA journal, 2000. **38**(4): p. 672-679.
67. Poggie, J., et al., *Quantitative visualization of compressible turbulent shear flows using condensate-enhanced Rayleigh scattering.* Experiments in Fluids, 2004. **37**(3): p. 438-454.
68. Smith, M. and A. Smits, *Visualization of the structure of supersonic turbulent boundary layers.* Experiments in Fluids, 1995. **18**(4): p. 288-302.
69. Maxwell, J.R. and G.B. Goodwin. *Large Eddy Simulation of Continuously Adjustable Hypersonic Wind Tunnel*. in *2018 Fluid Dynamics Conference*. 2018.
70. Aguilera Munoz, C., et al. *Characterization of Supersonic Wind Tunnel Flow Quality Using Planar Laser CO2 Rayleigh Scattering*. in *AIAA Propulsion and Energy 2021 Forum*. 2021.
71. Goldfeld, M.A., R.V. Nestoulia, and A.V. Starov, *The boundary layer interaction with shock wave and expansion fan.* Journal of Thermal Science, 2000. **9**(2): p. 109-114.

72. Arnette, S., M. Samimy, and G. Elliott, *Structure of supersonic turbulent boundary layer after expansion regions.* AIAA journal, 1995. **33**(3): p. 430-438.
73. Sabnis, K. and H. Babinsky, *Nozzle geometry effects on corner boundary layers in supersonic wind tunnels.* AIAA Journal, 2019. **57**(8): p. 3620-3623.
74. Gessner, F., *The origin of secondary flow in turbulent flow along a corner*. Journal of Fluid Mechanics, 1973. **58**(1): p. 1-25.
75. Gessner, F., S. Ferguson, and C. Lo, *Experiments on supersonic turbulent flow development in a square duct.* AIAA journal, 1987. **25**(5): p. 690-697.
76. Peltier, S.J., et al. *Structure of secondary motion in a Mach 2 boundary layer*. in *2018 AIAA Aerospace Sciences Meeting*. 2018.